Molecular Dynamics Analysis of Spectral Characteristics of Phonon Heat Conduction in Silicon

by,
Asegun Sekou Famake Henry

B.S., Mechanical Engineering (2004)
Florida A & M University

Submitted to the Department of Mechanical Engineering
in Partial Fulfillment of the Requirements for the Degree of
Master of Science in Mechanical Engineering

at the
Massachusetts Institute of Technology
June 2006

Signature of
Author...
Department of Mechanical Engineering
May 12, 2006

Certified
by...
Gang Chen
Professor of Mechanical Engineering
Thesis Supervisor

Accepted
by...
Lallit Anand
Chairman, Department Committee on Graduate Students

Molecular Dynamics Analysis of Spectral Characteristics of Phonon Heat Conduction in Silicon

by,

Asegun Sekou Famake Henry

Submitted to the Department of Mechanical Engineering
on May 12, 2006 in Partial Fulfillment of the
Requirements for the Degree of
Master of Science in Mechanical Engineering

Abstract

Due to the technological significance of silicon, its heat conduction mechanisms have been studied extensively. However, there have been some lingering questions surrounding the phonon mean free path and importance of different polarizations. This research investigates phonon transport in bulk crystalline silicon using molecular dynamics and lattice dynamics. The interactions are modeled with the environment dependent interatomic potential (EDIP), which was designed to represent the bulk phases of silicon. Temperature and phonon frequency dependent relaxation times are extracted from the MD simulations and used to generate a detailed picture of phonon transport. It is found that longitudinal acoustic phonons have the highest contribution to thermal conductivity and that the phonon mean free path varies by orders of magnitude with respect to the phonon spectra. For relaxation times, we observe moderate anisotropy and good agreement with the frequency dependence predicted by scattering theories. We also find that phonons with mean free paths between .1 and 10 micron are responsible for 50% of the thermal conduction, while phonons with wavelengths less than 10 nanometers make up 80%.

Thesis Supervisor: Gang Chen
Title: Professor of Mechanical Engineering

Acknowledgements

I would like to express my gratitude to professor Gang Chen for his support and guidance. I especially thank my parents and sister for their understanding and support throughout the MIT experience. Without them I would have no foundation. I must also express appreciation to my extended family and community for their encouragement. I also thank the Nanoengineering group members, who provided ideas, insight and assistance with research problems. I give special thanks to Erin for her love, support and reassurance during the highs and lows of this process. Finally thanks to Dean Colbert and the Department of Energy Computational Science Graduate Fellowship for their generous financial support.

Contents

List of Figures

Chapter 1: Introduction

Due to the limited supply of fossil fuels and their environmentally harmful byproducts, there is a global need for new energy technologies. Thermoelectrics are solid-state devices that convert energy directly between heat and electricity and could potentially be used in future renewable energy systems. Thermoelectrics are attractive because they can be used for both power generation and cooling applications. As solid-state devices, thermoelectrics are also reliable because they do not have any moving parts. Thermoelectrics are also scalable, so their efficiency is not size dependent.

Although thermoelectrics have attractive features, they are inefficient and inapplicable in most industries because they are not cost effective. Nanotechnological advances have created exciting new possibilities for enhancing thermoelectric efficiency, through the manipulation of quantum and classical size effects.[1] By increasing their efficiency, thermoelectrics may become cost effective and applicable to a wider variety of industries.

Among the naturally occurring materials, semiconductors such as silicon and its alloys, exhibit the highest thermoelectric efficiencies. Silicon is not only appropriate for thermoelectrics, but is also the base material for the microelectronics industry. As the backbone of most microelectronics, silicon's electrical and thermal properties have been extensively studied.[2-5] Despite the success of previous works,[6-12] questions surrounding the phonon mean free path and dominant conduction mechanisms continue to linger. In this work, we address some of the unresolved issues and present a methodology for analyzing lattice thermal conductivity. In this first chapter we start with a brief introduction to thermoelectric energy conversion and discuss how thermal conductivity reduction can improve efficiency. We then move to a discussion of thermal conductivity and conclude the chapter with an overview of strategies to improve thermoelectric efficiency.

1.1 Thermoelectric Energy Conversion

Thermoelectric energy conversion is based on the Seebeck and Peltier effects. The Seebeck effect can be observed by subjecting a material to a temperature gradient.[13]

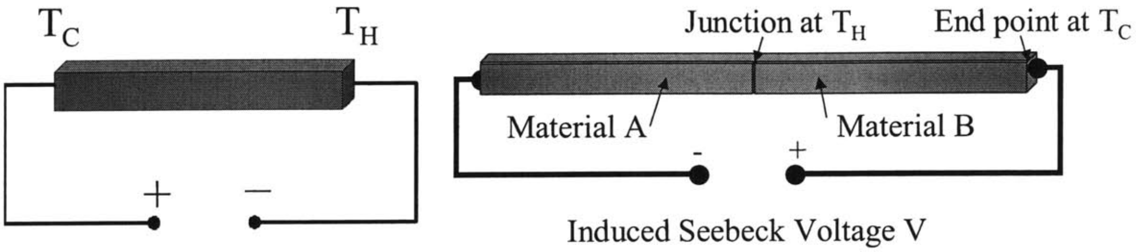

(a) (b)

Figure 1.1.1 (a) Single material subjected to a temperature gradient, (b) Dissimilar material junction subjected to temperature gradient

Figure 1.1.1 (a) illustrates the Seebeck effect, whereby conduction electrons diffuse away from the hot region to minimize their energy. The temperature gradient induces a transient current flow that increases the concentration of electrons in the colder region. In this transient process the electric potential in the cold region increases up to a level that prevents additional electrons from diffusing. This static potential is proportional to the temperature difference and is called the Seebeck voltage[14]

$$V = -\alpha \cdot \Delta T \tag{1.1.1}$$

where V is the Seebeck voltage, ΔT is the temperature difference from the hot to cold side and α is the Seebeck coefficient. The Seebeck voltage is related to the average energy carried by conducting electrons. Figure 1.1.1 (b) Illustrates how the Seebeck effect in two dissimilar materials is used for power generation. Since the materials have differing electron energy levels, a net voltage difference between the cold regions develops. This voltage difference is then used to supply power to an external circuit. The heat to electricity conversion process can also be reversed whereby an electrical current is passed and induces heating or cooling at each junction via the Peltier effect.

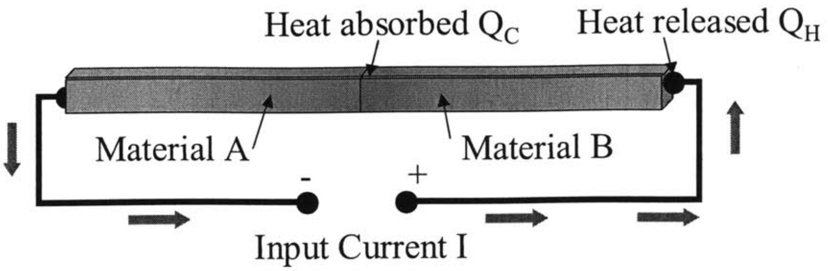

Figure 1.1.2 Illustration of Peltier effect

Figure 1.1.2 is an example of how one could observe the Peltier effect, whereby electrons either absorb or release heat at material junctions depending upon the direction of current flow. As electrons flow across a material junction they must change energy level in order to occupy an available state within their host material. The change in electron energy level is compensated by thermal energy in the local environment. Thus, if electrons cross a junction and decrease their energy, heat is transmitted to the local environment. On the other hand, if the electrons cross a junction and increase their energy, they cool the junction. The rate at which the junction is heated or cooled, Q, is proportional to the electrical current I by the Peltier coefficient Π[13]

$$Q = \Pi \cdot I \tag{1.1.2}$$

The Peltier coefficient is related to the Seebeck coefficient by, $\Pi = \alpha \cdot T$, and is associated with the average energy change electrons experience when crossing the junction.

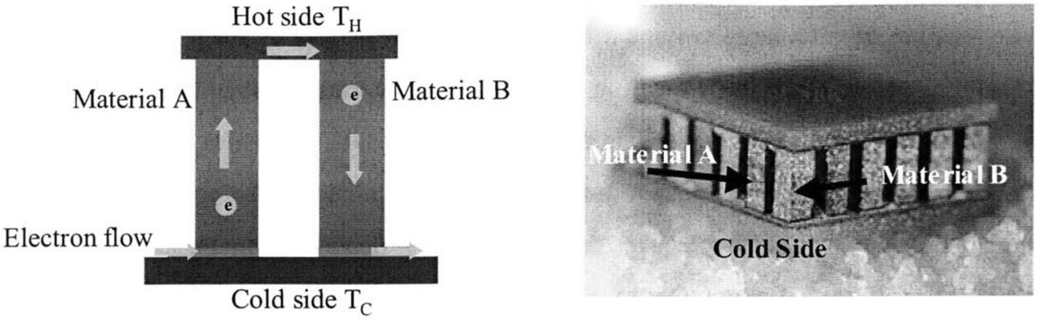

(a) (b)

Figure 1.1.3 (a) Typical layout of a thermoelectric junction, (b) Commercial thermoelectric device[15]

Figures 1.1.3 (a) and (b) illustrate the design of a typical thermoelectric junction and a commercial device that uses an array of junctions electrically connected in series. The major drawback to thermoelectrics is their efficiency, as the Seebeck coefficient of most materials is on the order of 10-100's of microvolts per degree temperature difference. Thus the challenge in making thermoelectrics more competitive lies in increasing their efficiency, given by the following relation[16]

$$\eta(ZT, T_H, T_C) = \left(\frac{\sqrt{ZT+1}-1}{\sqrt{ZT+1}+\frac{T_C}{T_H}} \right) \cdot \left(\frac{T_H - T_C}{T_C} \right) \tag{1.1.3}$$

where $\eta(ZT, T_H, T_C)$ is the ratio of electrical output power to heat input power, which depends on the hot and cold side temperatures T_H and T_C as well as a nondimensional constant called the figure of merit. The figure of merit ZT is a product of material properties Z and an average temperature T

$$ZT = \left(\frac{\alpha^2 \cdot \sigma}{\kappa} \right) \cdot T \tag{1.1.4}$$

where α is the Seebeck coefficient σ is electrical conductivity and κ is thermal conductivity. In a thermoelectric power generation device the goal is to achieve the largest ratio of voltage to temperature difference. To optimize the efficiency of thermoelectric devices the task reduces to increasing ZT, which is motivated by a few basic design criteria:

1. Increase α to get a large voltage difference for every degree of ΔT.
2. Increase σ so that joule heating is minimized, because joule heating is an irreversible loss that degrades efficiency.
3. Decrease κ so heat will not leak to the cold side and reduce ΔT.

Thus, the efficiency thermoelectrics is increased by designing materials with an appropriate combination of properties that enhance figure of merit. As a result most of the effort within the field of thermoelectrics is concentrated on materials development.

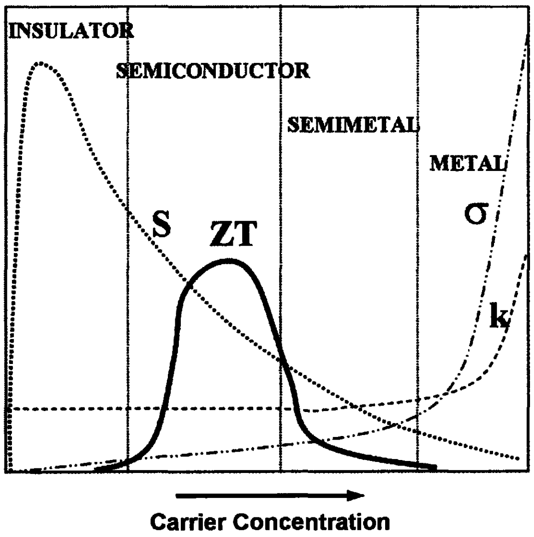

Figure 1.1.4 Material types and their corresponding figure of merit

Figure 1.1.4 shows that amongst naturally occurring materials, semiconductors exhibit the highest figure of merit. Semiconductors also have electrical properties that can be adjusted through doping, allowing for optimization flexibility. Interest in thermoelectrics has increased recently due to advances in nanotechnology, as researchers have developed ways to use quantum and classical size effects to enhance *ZT*.[1] As the characteristic length decreases, discrete electron energy levels become separated by larger gaps. This quantum size effect raises the average energy of conducting electrons and subsequently increases the Seebeck coefficient. The decrease in length scale also creates a classical size effect, whereby the phonon mean free path is affected by boundary scattering and reduces thermal conductivity.

The application of our research relates to the latter effect, which can decrease thermal conductivity without hindering electronic conduction. Few naturally occurring materials exhibit a high electrical to thermal conductivity ratio, however because the primary transport mechanism of electricity differs from heat in many materials, we can exploit them to engineer efficient materials. To set the stage for that discussion we first discuss thermal conductivity and the factors that determine its value.

1.2 Thermal Conductivity

In the early 1800's Joseph Fourier developed the macroscopic theory of heat conduction that is used today, whereby the heat flow in a material is proportional to the temperature gradient.[17]

$$\vec{\mathbf{Q}} = -\kappa \cdot \vec{\nabla} \cdot T \tag{1.2.1}$$

$\vec{\mathbf{Q}}$ is the heat flux vector, $\vec{\nabla} \cdot T$ is the temperature gradient and κ is the thermal conductivity. Fourier's law in a sense gives the definition of thermal conductivity that has been used extensively for macroscopic problems, where it is typically treated as a temperature dependent material property that is geometry independent. However, in emerging applications that involve nanomaterials, deviations from Fourier's law have been observed suggesting that additional theory is necessary.[18] Understanding of microscopic energy transport is essential to the development of heat transfer models for nanoscale applications.

At the microscopic scale, the picture of a material continuum breaks down and the picture of discrete atoms emerges. In crystalline solids this picture has highly repeated symmetry and forms a lattice where each atom is localized to a particular equilibrium position. In an idealized lattice all atoms are located at their lattice sites. The atoms experience a superposition of coulombic interactions with the charges of surrounding atoms, as any disturbance displaces an atom from its lattice site. In real crystals the atoms are constantly in motion, where the average kinetic energy is related to the local temperature, which will be justified later in chapter 3.

The mechanism of energy transport is the microscopic imbalance of energy. On average, the kinetic energy of atoms in a high temperature region is greater than a less excited cold region of a material. Interatomic forces transmit energy between atoms causing a net exchange of energy between hot and cold regions. The resultant energy diffusion occurs through a combination of interatomic forces and atomic diffusion. Fourier's law captures the direction of net energy exchange, through the direct proportionality between temperature gradient and heat flux. As a result Fourier's law is a valid formulation for macroscopic heat conduction, however nanostructured materials require geometric considerations.[18]

Energy transport is enhanced in most solids, as compared to liquids and gases, because crystal symmetries allow lattice waves to develop. Lattice waves are essentially sound waves within the solid, however the majority of waves oscillate with frequencies on the order of terahertz rendering them inaudible. In general sound waves in a solid decay at a rate proportional to the inverse square of the oscillation frequency. Most lattice waves have high frequencies and therefore decay faster than audible waves. However because these high frequency waves carry high energy, they are responsible for the majority of thermal transport in solids.

The development lattice waves can be described through a chain of effects occurring when an atom is displaced from its equilibrium position. The displaced atom experiences restoring forces from surrounding atoms that try to realign it to its lattice site. These forces, however, also act on the surrounding atoms and draw them away from their lattice site. The displacement transfers the initial perturbation to neighboring atoms causing waves to develop through a domino effect in the crystal. Waves transfer energy from an initially displaced atom to other atoms, as it eventually fades because each atom absorbs a portion of the initial perturbation energy. This simplified view of lattice waves is the basis for understanding energy transport in solids, as we later describe a method to quantify the energy, velocity and decay rate of the waves.

For the purpose of investigating transport phenomena we quantize the energy of waves and treat them as particles.[19] Quanta of lattice wave energy in solids are called phonons by analogy to photons, which are quantized electromagnetic waves. The connection between phonons and atoms is established through lattice normal modes, which are characterized by the crystal structure and interaction potential. For atoms in a crystal the forces are typically attractive at far distances due to bonding and repulsive at short distances due to coulomb repulsion from neighboring valence electrons. The simplest model of a solid involves generating the lattice assuming all the interactions are harmonic. The next level of detail would involve the addition of anharmonic, or non-quadratic terms to the potential. Anharmonic terms generate the nonlinear forces and vibrations that ultimately characterize a material's thermal conductivity. In the particle picture, the addition of anharmonicity introduces umklapp scattering,[19] whereby phonons to travel a finite distance before exchanging energy with another phonon.

An analogy between phonons in a solid and gas molecules in a container can be used to understand the temperature dependence of thermal conductivity. In solids energy transport occurs with phonons as primary energy carriers, similar to gasses where molecules are primary energy carriers. The basic principal of energy transport through particle diffusion can be illustrated using kinetic theory.

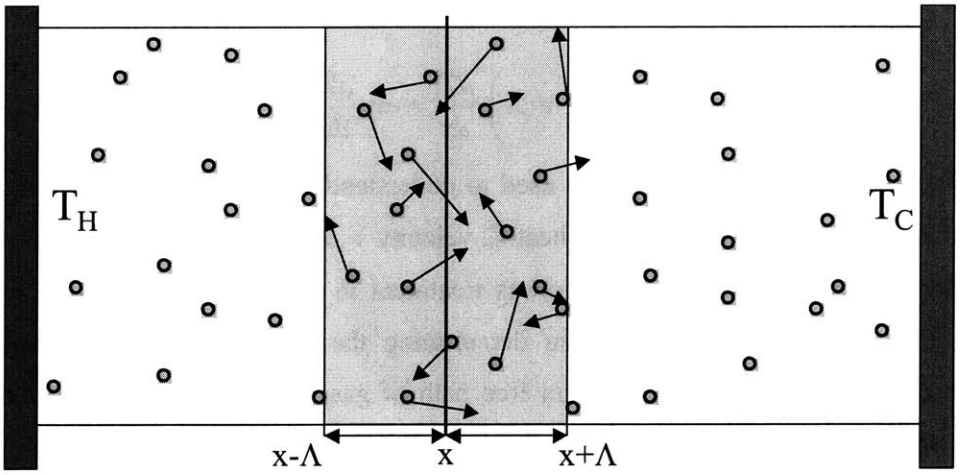

Figure 1.2.1 Kinetic theory model of energy transport in a gas

Figure 1.2.1 shows a cross section of gas molecules in a container with its walls at different temperatures. The molecules are moving randomly and some cross the boundary at location x, carrying their kinetic energy. By counting the number of molecules and their corresponding energy the net energy transport can be calculated as [20]

$$q_x = \frac{1}{2}\cdot\left(n\cdot E\cdot v_x\right)\Big|_{x-v_x\cdot\tau} - \frac{1}{2}\cdot\left(n\cdot E\cdot v_x\right)\Big|_{x+v_x\cdot\tau} \qquad (1.2.2)$$

where n is the number density and the factor of $\frac{1}{2}$ comes from assuming that roughly half the molecules move to the right and half move to the left. The x component of the velocity is v_x and τ is the average time a molecule travels before colliding and changing its trajectory. The atoms included in the counting must fall within the region of $\pm v_x \cdot \tau$, also called the mean free path Λ. Beyond a distance of one mean free path molecules tend to collide and change their trajectory before contributing to the transport in the x direction. Equation (1.2.2) can be written as a first order Taylor expansion and manipulated, assuming $\frac{1}{3}$ of the kinetic energy is associated with each velocity component. The result is an expression similar to Fourier's law, which yields a microscopic expression for thermal conductivity based on specific heat C, average velocity v and mean free path Λ.

$$q_x = -\left(\frac{1}{3}\cdot C\cdot v\cdot\Lambda\right)\cdot\frac{dT}{dx} = -\kappa\cdot\frac{dT}{dx} \qquad (1.2.3)$$

This resultant expression can be used to understand the transport of phonons in solids, where the phonons have specific heat C, velocity v, and mean free path Λ, as we derive the same result from a more rigorous treatment in chapter 3. The challenge in applying this model to phonons lies in determining the mean free path. A simple argument can be made to calculate mean free path of gas molecules that involves the diameter and number density. However in the case of phonons, the particle description of lattice waves does not have an analogous mean free path interpretation because phonons scatter by a mechanism not contained in the analogy.

Phonon scattering in the particle perspective is the result of lattice wave attenuation in the wave perspective. The destruction of coherent lattice waves in a crystal occurs through several mechanisms that reduce the phonon mean free path in the particle description. From the wave perspective these scattering mechanisms include anharmonicity, interface, impurity and surface obstructions. From the particle perspective these mechanisms correspond to umklapp, interface, impurity and surface scattering respectively.[19]

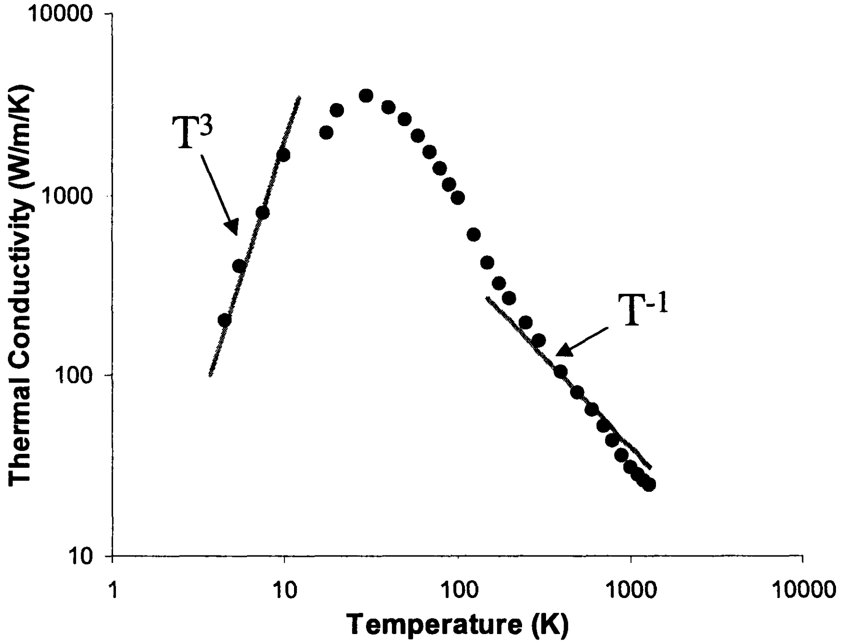

Figure 1.2.2 Thermal conductivity of silicon

Equation (1.2.3), however, can still be used to understand the temperature dependence of thermal conductivity in solids, illustrated in figure 1.2.2 for bulk silicon.[21] At low temperatures, phonon specific heat increases proportional to T^3, the velocity remains constant and mean free path is limited to the sample size, leaving the thermal conductivity proportional to T^3. At low temperatures atoms do not displace far from their equilibrium position, causing the potential interactions to approach harmonic. In the harmonic limit the phonons cease to interact and the thermal conductivity becomes infinite. However in experiments, boundary scattering limits phonon propagation to the sample's physical dimensions, leaving the mean free roughly constant. This effect, combined with diminishing specific heat at zero temperature, leads to the decay of thermal conductivity at zero temperature. As temperature increases specific heat increases and drives the thermal conductivity to its maximum value where the peak height depends on the purity and microstructure of the experimental sample.[19] High impurity or defect concentrations and smaller grain sizes reduce the height and position of the peak, as it occurs where umklapp scattering begins dominating. At higher temperatures the specific heat is roughly constant and umklapp scattering dominates decreasing the thermal conductivity roughly proportional to T^{-1}.

With the factors that determine thermal conductivity established we shift to discussion of strategies to decrease it, in order to optimize materials for thermoelectric applications. ZT can be increased by reducing κ, which contains both electron and phonon contributions. When a material is subjected to a temperature gradient, electrons also carry heat from hot to cold regions. In metals electron conduction plays a role in both charge and heat transport, making it difficult to decrease one without the other. However for semiconductors, the electron contribution is much smaller due to their low concentration and heat capacity. In order to decrease thermal transport, impurities can be added to scatter phonons, consequently reducing their mean free path.

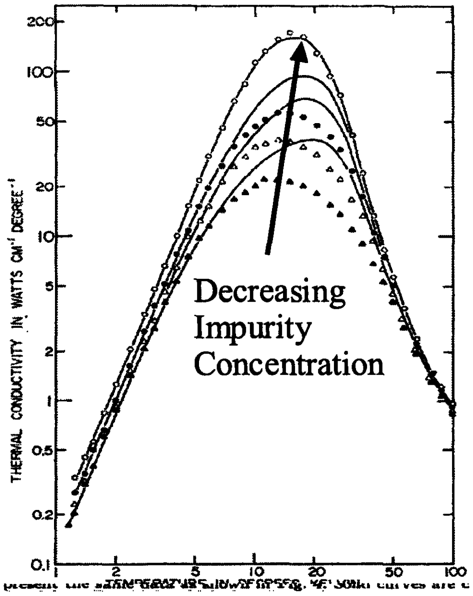

Figure 1.2.3 LiF Thermal conductivity at different impurity concentration[22]

Figure 1.2.3 shows experimental results for lithium fluoride where the thermal conductivity peak changes with impurity concentration.[22] This effect can be used to increase the electrical to thermal conductivity ratio by introducing impurities that have a similar electronic structure. In this technique phonon scattering is increased because lattice waves encounter atoms of different mass while electrons experience a similar electronic environment. By alloying bulk materials, studies have demonstrated the ability of this approach to increase thermoelectric efficiency.[23]

Another successful approach has been reduction of length scales, such that the phonon mean free path is decreased due to surface scattering.

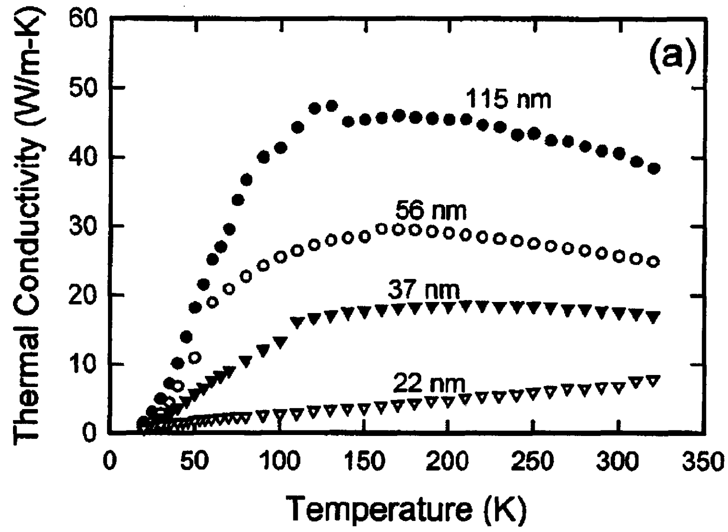

Figure 1.2.4 Classical size effect in silicon nanowires

In figure 1.2.4, classical size effects were experimentally observed for silicon nanowires.[24] Reducing characteristic dimensions in nanostructures confines phonons and hinders their ability to transport energy over large distances.

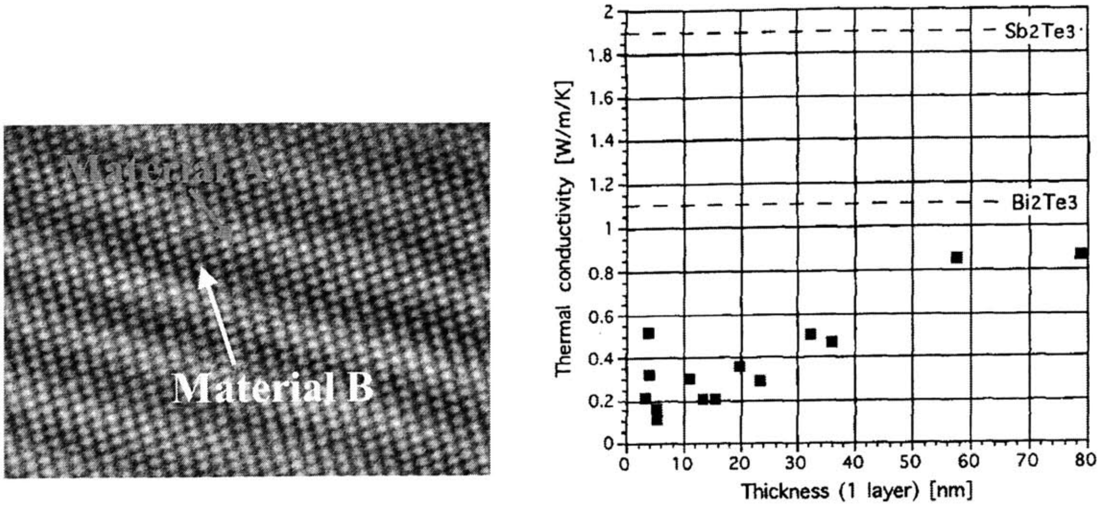

(a) (b)

Figure 1.2.5 (a) SiGe superlattice structure; (b) Bi_2Te_3 and Sb_2Te_3 superlattice thermal conductivity

Classical size effects can reduce thermal conductivity by orders of magnitude as it was also observed in superlattice structures, where alternating materials are grown in a periodic array. Figure 1.2.5 (a) shows a superlattice structure while figure 1.2.5 (b) shows thermal conductivity reduction as the layer thickness is decreased.[25] The periodic array of interfaces in superlattices reduces the phonon mean free path while preserving electrical conductivity to enhance *ZT*.

We now shift focus to the fundamental aspects of modeling phonon heat conduction. As indicated when introducing equation (1.2.3), modeling nanoscale heat transfer from a phonon perspective includes the task of determining phonon specific heat, velocity and mean free path. Although reasonable values for specific heat and velocity can be determined through experimental techniques, mean free path is not as straightforward. Klemens[19] pioneered an approach to calculate relaxation times using a quantum scattering matrix and Fermi's golden rule. By assuming linear dispersion, Klemens estimated the frequency and temperature dependence of relaxation times as $\tau \propto \omega^{-2} \cdot T^{-1}$. Although useful the approach requires fitting parameters to describe the relative contributions from each polarization.

Here we investigate silicon, which has been previously studied,[6-12] because of its technological significance. Accurately modeling silicon has proven difficult, while silicon's importance to the microelectronics industry creates a strong need for understanding its energy transport characteristics. In the following chapters we outline a method for modeling atomic motions in solids and quantifying phonon relaxation times and subsequent mean free paths. We first introduce the theory of molecular dynamics simulations and lattice dynamics. We then proceed by deriving analysis tools that are used to calculate thermal conductivity and extract relaxation times from molecular dynamics simulations. Subsequent chapters outline the simulation details and present our results for bulk silicon. Our approach allows us to determine the contributions from various phonon polarizations, bringing resolution to the thermal properties of a technologically significant material.

Chapter 2: Molecular Dynamics Simulations and Lattice Dynamics

In the first chapter we discussed the significance of thermal conductivity in strategies to increase thermoelectric figure of merit. We also discussed length scales where thermal conductivity becomes a size dependent property. Here we introduce a numerical method called molecular dynamics (MD), used to investigate fundamental mechanisms and characteristics of materials. Although MD simulations can be used to study a wide variety of phenomena, our investigation focuses on the phonon mean free path, which is related to the decay rate of lattice waves in solids. In this chapter we introduce the theory of MD simulations and lattice dynamics and discuss how they can be implemented.

2.1 The Theory of Molecular Dynamics Simulations

In classical mechanics the trajectory of a body with rigid or deformable shape is determined through classical equations of motion. Under the classical framework a body's position, velocity and acceleration are calculated deterministically in response to driving forces. By contrast, quantum mechanics treats material bodies probabilistically, as waves whose spatial extent is determined through a Hamiltonian operator. In the classical framework bodies cannot occupy the same space, however under the quantum framework individual material waves can interfere leading to interesting phenomena.[26] In general quantum mechanical descriptions of material bodies are more complicated, but include quantum wave effects that can dominate at atomic scales.

To model atomic motion in solids it is important know if quantum wave effects can be neglected. MD simulations model the motion of atoms in a substance by treating atoms as point particles, using classical equations of motion to calculate their trajectory. For MD simulations, the point particle treatment validity can be checked by comparing the De Broglie wavelength of an atomic nucleus to the atomic separation. For silicon at room temperature, the nucleic wavelength is only .02 nm, an order of magnitude smaller than the lattice constant. Thus, material wave effects can be neglected and the particle treatment should accurately represent the dynamics above room temperature. At low temperatures, however, this assumption becomes questionable because the wavelength extends between atoms and interference effects are important.

MD simulations track the trajectory of particles by sequentially integrating the equations of motion to determine positions after fixed time intervals.[27] In classical MD simulations Newtonian dynamics are used to relate forces to particle accelerations through

$$\vec{\mathbf{F}} = m \cdot \frac{d^2\vec{\mathbf{r}}}{dt^2} \tag{2.1.1}$$

where $\vec{\mathbf{F}}$ is force, m is its mass and $\frac{d^2\vec{\mathbf{r}}}{dt^2}$ is the particle acceleration. In MD simulations forces are calculated from a potential energy model. A potential energy model is the most important component, because its accuracy in describing the interactions will determine the accuracy or realism of the results. Most often potential models are functions of atomic positions and do not include velocity contributions. This is because most models are an effective treatment of coulombic interactions. Once potential energy function Φ has been established the force on a particle can be determined by

$$\vec{\mathbf{F}}_i = -\frac{\partial \Phi}{\partial \vec{\mathbf{r}}_i} \tag{2.1.2}$$

where $\vec{\mathbf{F}}_i$ is the force on a particle labeled i. The force to energy relationship in (2.1.2) ensures that particles adjust their position to minimize the system's potential energy. With the potential model, initial positions and velocities specified, the force on each particle is calculated numerically. Using the positions velocities and calculated forces, future positions of particles are predicted using an algorithm to integrate the equation of motion. The simplest and most popular is the Verlet algorithm,[27] based on a forward and backward Taylor expansion of a particle position in time. By adding,

$$\vec{\mathbf{r}}_i(t+\Delta t) = \vec{\mathbf{r}}_i(t) + \vec{\mathbf{v}}_i(t)\cdot \Delta t + \frac{\vec{\mathbf{F}}_i}{2\cdot m_i}\cdot(\Delta t)^2 \tag{2.1.3}$$

and

$$\vec{\mathbf{r}}_i(t-\Delta t)=\vec{\mathbf{r}}_i(t)-\vec{\mathbf{v}}_i(t)\cdot\Delta t+\frac{\vec{\mathbf{F}}_i}{2\cdot m_i}\cdot(\Delta t)^2 \tag{2.1.4}$$

we can arrive at

$$\vec{\mathbf{r}}_i(t+\Delta t)=2\cdot\vec{\mathbf{r}}_i(t)-\vec{\mathbf{r}}_i(t-\Delta t)+\frac{\vec{\mathbf{F}}_i}{m_i}\cdot(\Delta t)^2 \tag{2.1.5}$$

where the velocity is calculated as

$$\vec{\mathbf{v}}(t)=\frac{\vec{\mathbf{r}}_i(t+\Delta t)-\vec{\mathbf{r}}_i(t-\Delta t)}{2\cdot\Delta t} \tag{2.1.6}$$

$\vec{\mathbf{r}}_i(t+\Delta t)$ is the particle's predicted position, $\vec{\mathbf{r}}_i(t)$ is its current position, $\vec{\mathbf{r}}_i(t-\Delta t)$ was its previous position, $\vec{\mathbf{v}}(t)$ is its velocity, $\frac{\vec{\mathbf{F}}_i}{m_i}$ is its acceleration and Δt is the specified time interval. Since the velocity is calculated based on the predicted position, obtained from the algorithm itself, the Verlet algorithm is generally more stable than the forward or backward schemes alone. This is because it uses the acceleration, current and previous positions as inputs and not the velocity, which contains numerical error from the current timestep. With this scheme future positions are computed iteratively to determine a system's trajectory. More stable and accurate algorithms exist, however they have increased complexity and computational expense. Other algorithms such as the Verlet leapfrog only provide velocities at half timesteps, which can be problematic when evaluating velocity dependent properties.[28]

The last component to MD simulations is the specification of initial and boundary conditions. Typical simulations start with particles at random positions and initial velocities that correspond to a desired temperature. It is this natural inclusion of temperature that makes MD ideal for the investigation of temperature dependent phenomena. The specification of boundary conditions depends on the problem of interest, but wherever possible it is typical to impose periodic boundary conditions to imitate an infinite medium. Periodic boundaries are useful because the size and timescale of MD simulations are the limiting factors in its implementation. A periodic boundary is a natural condition that reflects microcanonical statistics, as it inherently conserves the number of particles, energy and volume.[27]

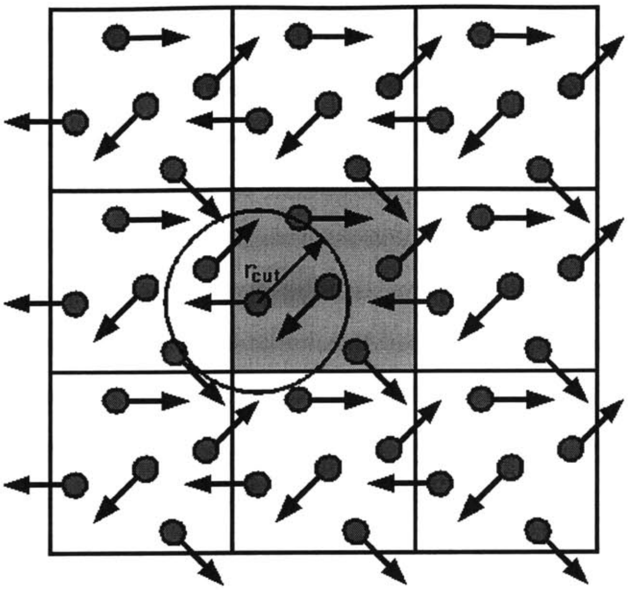

Figure 2.1.1 Illustration of periodic boundary condition

Figure 2.1.1 shows how periodic boundary conditions are implemented in a two-dimensional simulation domain. As atoms move beyond boundaries they reenter through opposite sides so that the particle interactions are geometrically cyclic, preserving energy and volume in a simulation cell. Periodic boundaries are easily implemented by copying particle positions such that atoms on one side of the domain interact with atoms on the opposite side. This is a feature that naturally works with rectangular cells, the most common domain shape.

Other boundary conditions have been developed for simulating constant temperature and constant pressure ensembles that involve rescaling the equations of motion.[20] Boundary conditions that correspond to equilibrium statistical ensembles maintain thermal equilibrium, however the choice of boundary condition can also be used to simulate nonequilibrium systems. Techniques for equilibrium and nonequilibrium simulations have been developed, each with its own advantages and drawbacks. Nose-Hoover thermostats[29] and velocity rescaling are nonequilibrium boundary conditions that alter atomic trajectories to impose heat fluxes and induce temperature gradients. Using this approach thermal conductivity is calculated by inverting the temperature gradient in accordance with Fourier's law.

Although the thermal conductivity calculation is intuitive, nonequilibrium techniques have a few drawbacks, as the vibration of atoms becomes unnatural in regions where the boundary conditions are applied. When applying nonequilibrium techniques, vibration dynamics in boundary regions are no longer solely governed by the interatomic potential and velocity modifications introduce additional phonon scattering. In nonequilibrium simulations, properties such as thermal conductivity, which are based on phonon scattering, are affected in ways that become difficult to quantify. In many studies,[30-36] computational limitations lead to simulation domains nanometers in length, which become problematic when generating a temperature gradient. If the domain is small, large heat fluxes on the order of MW/m^2 are required to generate measurable temperature differences. This also introduces problems in establishing a steady state temperature profile. By contrast, equilibrium techniques allow for natural atomic vibration without boundary artifacts introduced by trajectory modifications. A common drawback to equilibrium techniques is the necessity for long time simulations to allow full dissipation of statistical fluctuations. In our case this disadvantage is alleviated by access to sufficient computational resources. As a result we used equilibrium MD for our thermal conductivity calculations, which allowed greater flexibility in our analysis of atomic vibrations without infringing artifacts.

2.2 Interatomic Potentials

In the previous section we outlined the general methodology of MD simulations without heavily focusing on the most important aspect, the potential energy model. The potential energy model is the essential feature of MD simulations that determines the dynamics and results. Potential models generally fall between two categories, quantum or empirical. In general, modeling interactions involves approximate solution of nonlinear N-body problems, where speed and simplicity in empirical models is traded at the expense of accuracy and realism in quantum models. In MD simulations the most expensive portion of the program is calculating the forces. As a result MD simulations are limited by processor speed as opposed to available memory. Hence, careful considerations should be taken when choosing a potential model so that an optimal balance of accuracy and speed is achieved.

What we have referred to, as a quantum potential model is often called ab initio or first principals calculation. This highly accurate, quantum mechanical description of interatomic interactions involves numerically solving the N-body time independent Schrodinger equation for the electronic wave function. Its accuracy is accompanied by extremely large computational expense by comparison to both semi and empirical methods.

Ab initio calculations have become popular in recent years due to advancements by Walter Kohn and John Pople, who received a Nobel prize in 1998 for developing density functional theory (DFT).[37] In DFT the assumption is made that all electrons occupy their ground state and the Schrodinger equation is solved for a pseudo-electron wave function. In DFT the valence electrons are treated as degrees of freedom, while the core electrons and nuclei are represented by pseudopotentials. Under this approach, the electronic structure of virtually any material can be determined. By knowing the electronic structure, highly accurate forces can be calculated based on very few underlying assumptions. Excellent agreement between DFT calculations and experiments has been observed for a variety of material properties.[38-41] In quantum molecular dynamics (QMD) the wave function is recalculated after every timestep, which currently limits the size and length of simulations to a few hundred atoms and picoseconds. These limitations render QMD inappropriate for our purposes, however as computer hardware advances it may eventually become a feasible option.

Other semi-empirical techniques, such as tight binding[42] and learn on the fly,[43] lie in between quantum and classical models with varying accuracy and computational expense. Nevertheless we shift our focus to classical potentials, which have the least computational expense, as we will see our application requires multiple nanosecond simulations. Since empirical potentials were developed before DFT, they have been widely used in molecular dynamics applications. In general, an empirical potential is developed by first creating a physically motivated functional form. Potential parameters embedded in the form are then fit, minimizing the error between the model and experimental data. In many cases, a functional form is developed for a certain type of bonding, usually based on a physical observation or conjecture about electron states or effective coulomb interactions. Once the functional form is chosen, parameters are fit by comparing properties calculated using the potential, to a variety of experimental data and more recently to QMD forces via the force matching method.[44]

One of the mostly widely used empirical potentials was developed by Lennard and Jones and is commonly called the Lennard-Jones or LJ potential. This potential's functional form was physically motivated by the separation dependence of dipole interactions. In dipoles, positively charged nuclei experience a screened attraction to the electrons of surrounding atoms. By summing these coulombic contributions it can be determined that the attractive potential between two neighboring dipoles decays as $\frac{1}{\|\vec{\mathbf{r}}\|^{6}}$, with $\|\vec{\mathbf{r}}\|$ equal to the dipole separation. As a result, the famous Lennard-Jones 6-12 potential for a system of N dipoles was developed with the following functional form,

$$\Phi = \sum_{i=1}^{N} \sum_{\substack{j=1 \\ j \neq i}}^{N} -4 \cdot \varepsilon \cdot \left[\left(\frac{\sigma}{\|\vec{\mathbf{r}}_{ij}\|} \right)^{6} - \left(\frac{\sigma}{\|\vec{\mathbf{r}}_{ij}\|} \right)^{12} \right] \tag{2.2.1}$$

where Φ is the potential energy, the subscripts i and j are used to label different atoms, ε is the minimum energy, σ is a length scale and $\|\vec{\mathbf{r}}_{ij}\|$ is the dipole separation. The 12th power term in the potential represents the repulsive interactions that dominate at very close distances and keep atoms from fusing together.

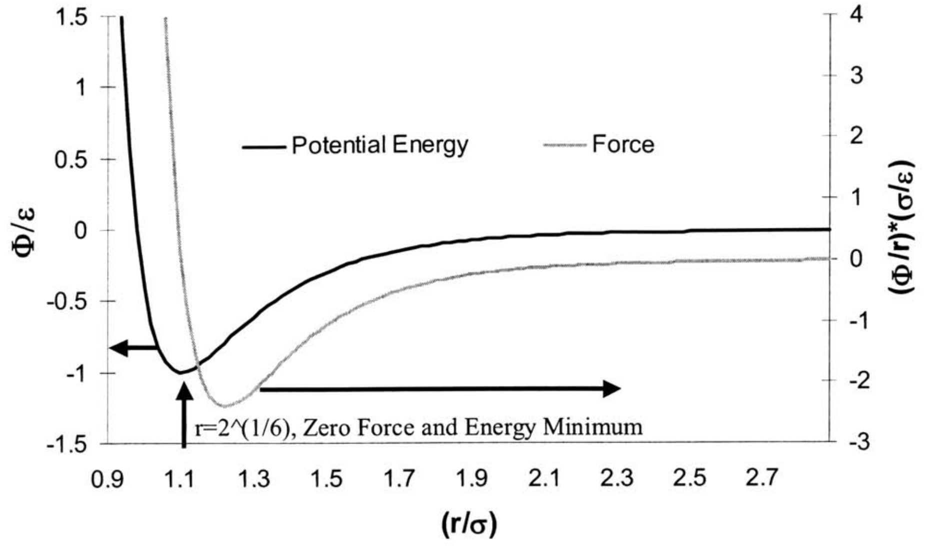

Figure 2.2.1 Lennard-Jones potential and force

Figure 2.2.1 shows a plot of the Lennard-Jones potential and force as a function of increasing distance. The forces are largely repulsive at short distances and decrease to zero at the equilibrium distance $\sigma^{\frac{1}{6}}$, where the repulsion is balanced by attraction. Beyond that distance, forces are weakly attractive but extend out to infinity. Balancing attractive and repulsive forces is a standard approach for empirical potential development, as most models include an attractive term that dominates for large separation and a repulsive term for short distances when valence electrons shells overlap. The Lennard-Jones potential has been widely used and has shown the best agreement with noble gases, since their electron shells are completely filled and the bonding amongst atoms is dominated by Van der Waals forces.

There are many other materials in nature that cannot be described simply by Van der Waals interactions. Some of these materials, however, can still be described using a pair attraction and repulsion scheme. Successful models for metals were developed using a pair potential scheme called embedded atom method (EAM).[45] This methodology was motivated by the physical understanding that metals have conduction electrons that are weakly bonded to individual atoms. EAM assumes a fixed functional form for a pseudo-electron density, whereby an atom's potential is calculated by superimposing electron densities of neighboring atoms. This method has been successful in describing the properties of some metals and only requires the computational expense of a pair potential.

Despite the successes of pair potentials, there are still many elements that cannot be described using a summation of pair interactions. Semiconductors in particular tend to be covalently bonded, which induces angular forces. Due to the complexity of covalent bonds, semiconductors such as silicon are particularly difficult to model. The electronic band structure of semiconductors gives them important properties that are exploited particularly in the electronics industry, however these properties are difficult to model with a transferable closed form representation. In the case of silicon there have been many attempts to accurately model its behavior with moderate successes. The most important feature that is commonly characteristic of silicon potentials is that of a three-body term that contributes angular forces. It has been found that this term is necessary for stabilizing the diamond phase of silicon and is generally a fundamental component in modeling covalent solids.

Some of the best recognized pioneering efforts in modeling silicon include the Stillinger-Weber and Tersoff potentials.[46,47] Stillinger and Weber's potential is designed to stabilize the diamond structure by penalizing atoms for deviating from the prescribed nearest neighbor angle of 109 degrees. By contrast, Tersoff's potential is designed like a pair potential, where the attractive term's coefficient has three-body dependence. Thus the three-body angular effects are implicitly included via coordination variable that counts contributions from neighboring atoms. One aspect of these three body potentials that makes them computationally manageable is the inclusion of a nearest neighbor cut-off function that truncates the interactions beyond first neighbors. This is quite different from a Lennard-Jones pair potential, where third and fourth nearest neighbors are sometimes included.

2.3 The Environment Dependent Interatomic Potential

The environment dependent interatomic potential (EDIP),[48] introduced a new functional form with added complexity yet comparable cost to previous three-body models for silicon. Some of the functions within the potential are physically motivated by closed form quantum mechanical results as it was targeted to represent the bulk phases of silicon. We have chosen this potential for our study because of the extensive considerations involved in its functional form, where explicit coordination dependence is included. The coordination number of an atom is a measure of how many nearest neighbors it has. Coordination dependence is particularly important for covalently bonded atoms, because when coordination increases the valence electrons are shared amongst more atoms and the bonding between any two atoms weakens. Studies have shown[49] that the cohesive energy per atom increases proportional to $Z^{\frac{1}{2}}$ where Z is the coordination. The inclusion of explicit coordination dependence is an important feature that distinguishes EDIP from other silicon potentials. Here we review its major features to justify our motives in selecting it for our bulk silicon MD simulations.

EDIP has an explicit pair and three-body summation where the energy is written in terms of a single atom as opposed to pairs or triplets. The energy of each atom is given by

$$E_i = \sum_{j \neq i} V_2(r_{ij}, Z_i) + \sum_{\substack{j>k \\ j \neq i \\ k \neq i}} V_3(r_{ij}, r_{ik}, l_{ijk}, Z_i) \tag{2.3.1}$$

where E_i is the energy of an atom labeled i, V_2 is a pair potential, V_3 is a three-body potential energy, $\vec{\mathbf{r}}_{ij}$ is the displacement vector $\vec{\mathbf{r}}_i - \vec{\mathbf{r}}_j$, $\vec{\mathbf{r}}_{ik}$ is the vector between i and k and Z_i is the scalar coordination number. The pair summation is over all possible atoms j not equal to i, while the triplet summation is over unique triplets ijk with each combination counted once. The pair potential represents the strength of an ij bond, while the three-body potential represents preferences to certain bond angles due to hybridization and provides angular forces to resist deviation from those configurations. The pair and three body potentials have the following functional form.

$$V_2(r_{ij}, Z) = A \cdot \left[\left(\frac{B}{r_{ij}} \right)^{\rho} - p(Z) \right] \cdot \exp\left(\frac{\sigma}{r_{ij} - a} \right) \tag{2.3.2}$$

$$V_3(r_{ij}, r_{ik}, l_{ijk}, Z) = g(r_{ij}) \cdot g(r_{ik}) \cdot h(l_{ijk}, Z_i) \tag{2.3.3}$$

V_2 goes to zero at a cut off distance a, truncated beyond the nearest neighbor and V_3 goes to zero at b through the radial function $g(r)$, while $p(Z)$ represents the bond order, which has a functional form motivated by quantum mechanical results. Most of the physics that distinguishes EDIP is contained in the angular function $h(l_{ijk},Z)$. The radial and bond order functions are

$$g(r) = \exp\left(\frac{\gamma}{r-b}\right) \tag{2.3.4}$$

$$p(Z) = \exp(-\beta \cdot Z^2) \tag{2.3.5}$$

$$l_{ijk} = \frac{\vec{\mathbf{r}}_{ij} \cdot \vec{\mathbf{r}}_{ik}}{\|\vec{\mathbf{r}}_{ij}\| \cdot \|\vec{\mathbf{r}}_{ik}\|} \tag{2.3.7}$$

$$Z_i = \sum_{m \neq i} f(r)$$

$$f(r) = 1 \qquad \text{if } r < c,$$

$$f(r) = \exp\left(\frac{\alpha}{1-\frac{1}{x^3}}\right) \qquad \text{if } c < r < b, \qquad x = \frac{(r-c)}{(b-c)},$$

$$f(r) = 0 \qquad \text{if } r > b \tag{2.3.8}$$

where l_{ijk} is the triplet bond angle and the function $h(l_{ijk},Z)$ has a few physically motivated properties embedded in its form. The function $h(l_{ijk},Z)$ contains two coordination dependent functions $\tau(Z)$ and $Q(Z)$. Both functions are embedded in $h(l_{ijk},Z)$ such that $\tau(Z)$ controls the preferred bonding angles while the stiffness is controlled by $Q(Z)$, which decreases as coordination increases in the covalent to metallic transition. The angular function $h(l_{ijk},Z)$ has a zero minimum when $l_{ijk} = -\tau(Z)$ and is flat away from the minimum, which gives very weak forces for large angular distortions. The coordination dependence in this function is physically motivated by the understanding that when covalent bonds are bent far from equilibrium they are weakened and form new electron states. The angular function $h(l_{ijk},Z)$ has the following form

$$h\left(l_{ijk},Z\right)=\lambda\left[\left(1-\exp\left(-Q(Z)\cdot\left(l_{ijk}+\tau(Z)\right)^{2}\right)\right)+\eta\cdot Q(Z)\cdot\left(l_{ijk}+\tau(Z)\right)^{2}\right] \quad (2.3.8)$$

$$Q(Z)=Q_{0}\cdot\exp\left(-\mu\cdot Z^{2}\right) \quad (2.3.9)$$

$$\tau(Z)=u_{1}+u_{2}\cdot\left(u_{3}\cdot\exp\left(-u_{4}\cdot Z\right)-\exp\left(-2\cdot u_{4}\cdot Z\right)\right) \quad (2.3.10)$$

where the constants in $\tau(Z)$ were determined from ab initio calculations. With this functional form, the potential was fit to a database of experimental and ab initio results. The emphasis for the fitting set was placed on the elastic constants, vacancy energies and inversion of ab initio energy curves or force profiles along high symmetry directions. EDIP has shown good agreement with experimental results and was thus a justifiable choice of potential for our study.

2.4 Lattice Dynamics

In addition to using MD, we used lattice dynamics to determine the phonon density of states and polarization vectors. Lattice dynamics is a generalized formulation that can provide a useful picture into the spectral characteristics of phonons. To introduce the formulation we take a simple one-dimensional chain as an example and then move to a more general formulation involving the solution of an eigenvalue equation.[50]

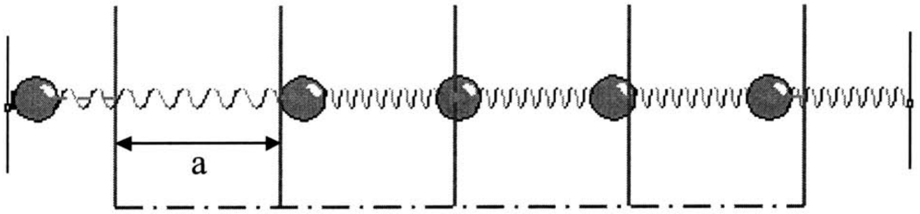

Figure 2.4.1 One-dimensional chain of atoms

Consider the one-dimensional chain of atoms in figure 2.4.1, where every atom is connected with a spring to two neighboring atoms on each side. If we sum the forces and write down the equation of motion for the nth atom in the chain, we have the following wave equation

$$m_{n}\cdot\frac{d^{2}u_{n}}{dt^{2}}=K\left(u_{n+1}-u_{n}\right)-K\left(u_{n}-u_{n-1}\right)\Rightarrow m_{n}\cdot\frac{\partial^{2}u_{n}}{\partial t^{2}}=Ka^{2}\frac{\partial^{2}u_{n}}{\partial x^{2}} \quad (2.4.1.)$$

where u_n is the displacement from equilibrium, the subscript n denotes its position in the chain, K is the spring constant, $\frac{\partial^2 u_n}{\partial t^2}$ is the acceleration and m is the mass of the atom. If we assume the chain to be infinite, taking the continuum limit, we arrive at the second expression in 2.4.1 solved by a series of plane waves

$$u_n = A \cdot \exp(-i \cdot (\omega \cdot t - k \cdot n \cdot a)) \qquad (2.4.2)$$

where k is a wavevector equal to $\frac{2\pi}{\lambda}$, where λ is a wavelength corresponding to the wave's spatial periodicity while ω is the vibrating frequency. Plugging the solution back into 2.4.1 we arrive at expression for the mode frequencies as a function of wave vector, or dispersion relation.

$$\omega = 2\sqrt{\frac{K}{m}} \cdot \left|\sin\left(\frac{k \cdot a}{2}\right)\right| \qquad (2.4.3)$$

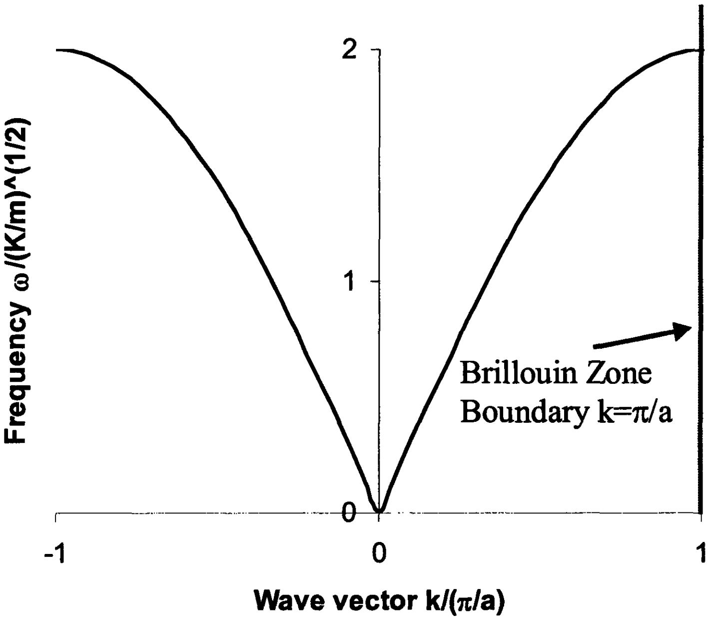

Figure 2.4.2 Dispersion relation for the one-dimensional chain

A few properties of the dispersion relation shown in figure 2.4.2 include, a periodic solution in k and upper limit to the frequency at $2\sqrt{\frac{K}{m}}$. This simplified case shows that when masses are connected together with long-range repetition, frequencies lower than the natural pair oscillator frequency appear in the temporal displacement of each atom. The periodic solution in k illustrates an important symmetry property, such that the highest unique k vector occurs at $k = \frac{\pi}{a}$. Shorter wavelengths beyond this k value, called the first Brillouin zone boundary, reproduce the same atomic displacements as longer wavelengths occurring within the first Brillouin zone. Thus, the Brillouin zone represents the shortest range of k vectors that correspond to unique periodicity in atomic displacements.

We now generalize the above treatment to three dimensions and more than one basis atom. Rewriting 2.4.3 in matrix form for a single term in the infinite series plane wave solution we arrive at the following[50]

$$\omega^2(\vec{\mathbf{k}},\nu)\cdot\vec{\mathbf{e}}(\vec{\mathbf{k}},\nu) = \mathbf{D}(\vec{\mathbf{k}})\cdot\vec{\mathbf{e}}(\vec{\mathbf{k}},\nu) \tag{2.4.4}$$

where $\vec{\mathbf{e}}(\vec{\mathbf{k}},\nu)$ is a complex vector representing the polarization direction for the mode and $\mathbf{D}(\vec{\mathbf{k}})$ is the dynamical matrix containing the mass and stiffness information as it relates to a particular propagation direction. The elements of the dynamical matrix are generalized for more than one basis atom. A separate basis atom can correspond to the same species, as is the case for silicon, where the elements of the matrix are given by[50]

$$\mathbf{D}_{\alpha\beta}(jj',\vec{\mathbf{k}}) = \frac{1}{(m_j \cdot m_{j'})^{\frac{1}{2}}}\cdot\sum_{l'}\phi_{\alpha\beta}(jj',0l')\cdot\exp\left(i\cdot\vec{\mathbf{k}}\cdot\left[\vec{\mathbf{r}}(j'l') - \vec{\mathbf{r}}(j0)\right]\right) \tag{2.4.5}$$

$$\phi_{\alpha\beta}(jj',0l') = \frac{\partial^2\Phi}{\partial u_\alpha(jl)\partial u_\beta(j'l')} \tag{2.4.6}$$

The indices j and j' label individual atoms while l identifies the unit cell the atom is in. The dynamical matrix is symmetric and Hermitian, guaranteeing real eigenvalues that are all positive for stable crystal structures. The eigenvectors, however, may be complex. The real and imaginary parts of each eigenvector correspond to the coefficients of an elliptically polarized wave, the most general way to express plane waves.

Generalization of 2.4.5 to more arbitrary basis allows for additional solutions for frequency and polarization vectors. When applied to three-dimensional lattices, at least three eigenvalues and eigenvectors result from the matrix equation 2.4.4. These solutions create additional branches in the dispersion, as two solutions are associated with out of plane motion and one is associated with in plane motions. These branches of solutions are subsequently called transverse and longitudinal acoustic vibration modes respectively, where the polarization vector $\vec{\mathbf{e}}(\vec{\mathbf{k}},\nu)$ in 2.4.4 describes the displacement direction. In the case of diamond structured silicon we have two basis atoms, a 6x6 dynamical matrix and six solutions. The three additional solutions also correspond to in and out plane vibrations, however they are associated with relative vibrations between basis atoms. The relative displacements between basis atoms give rise to higher frequencies called transverse and longitudinal optical modes. Of these six branches we seek their relative contributions to thermal conductivity, as we outline a method for analyzing their dynamics in chapter 3.

Equation 2.4.6 expresses the essential assumption of lattice dynamics, which is the harmonic limit of the potential model. By Taylor expanding the potential the first derivative term cancels out for equilibrium structures because the net forces are zero. The second derivative, however, is nonzero and can be interpreted as a harmonic or spring constant model of a given potential in the equilibrium structure. Essentially, the harmonic approximation in lattice dynamics describes the limiting characteristics of the potential, when subjected to an infinitesimal perturbation. Classically the static lattice corresponds to zero temperature, as the phonon frequencies we observe in finite temperature MD simulations are expected to be lower than those predicted by lattice dynamics. In our analysis we neglect this discrepancy between zero and finite temperature, using the mode polarization vectors from lattice dynamics to decompose the motions of atoms from MD into normal mode coordinates. Using these tools we now address the analysis of a MD trajectory and build a framework to determine phonon mean free path.

Chapter 3: MD Simulation Analysis

In the previous chapter we introduced the theory and methodology of MD simulations and here we describe the analysis of a MD trajectory to extract thermal properties. After setting initial and boundary conditions, particles are sequentially stepped forward in time. At first glance the trajectory appears random, but when viewed through a statistical lens, patterns emerge. The statistical patterns contain information about a material's temperature dependent response to perturbations. In this chapter we cover six derivations that set a premise for trajectory analysis. These analysis tools can be used to calculate thermal conductivity and identify its phonon frequency dependent contributions.

3.1 Energy and Temperature

As discussed in chapter 2, an equilibrium MD simulation with periodic boundary conditions naturally conserves energy, volume and the number of particles. These conserved quantities correspond to the microcanonical statistical ensemble, where the energy in the simulation is

$$E = \Phi + \sum_{i=1}^{N} \frac{1}{2} \cdot m_i \cdot \vec{\mathbf{v}}_i^{\,2} \tag{3.1.1}$$

Φ is the system potential energy, m_i is the particle mass, $\vec{\mathbf{v}}_i$ is its velocity and the system energy E remains constant. The second term in (3.1.1) is the system's kinetic energy, as we show it is consistent with 2.1.1 by taking the time derivative of the energy

$$\frac{dE}{dt} = \sum_{i=1}^{N} \frac{\partial \Phi}{\partial \vec{\mathbf{r}}_i} \cdot \frac{\partial \vec{\mathbf{r}}_i}{\partial t} + \frac{1}{2} \cdot m_i \cdot \left(2 \cdot \vec{\mathbf{v}}_i \cdot \frac{\partial \vec{\mathbf{v}}_i}{\partial t} \right) = 0$$

$$-\frac{\partial \Phi}{\partial \vec{\mathbf{r}}_i} = m_i \cdot \left(\frac{\partial \vec{\mathbf{v}}}{\partial t} \right) \tag{3.1.2}$$

Thus, $\frac{1}{2} \cdot m \cdot \vec{\mathbf{v}}^2$ conserves the total energy when calculating the forces as $-\frac{\partial \Phi}{\partial \vec{\mathbf{r}}_i}$. The deviation in energy is most often a first debugging check when writing a MD code, where total energy fluctuations are usually on the order of .01% of the initial energy per atom. With this definition for energy we now describe the system temperature.

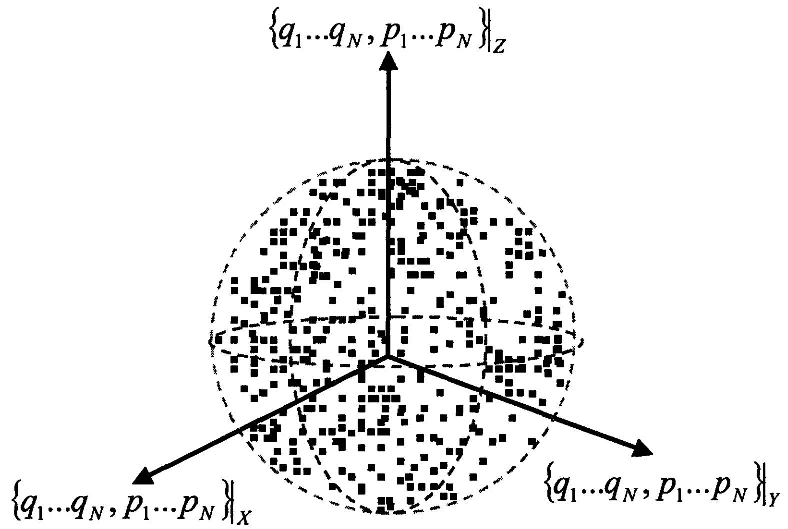

Figure 3.1.1 Depiction of microscopic systems in phase space

To determine the temperature of a system of particles we must relate their positions and momenta to macroscopic variables we observe. Intuitively we know that for the same macroscopic state, described by its temperature, pressure, volume, etc. we have a large number of corresponding microscopic states. If we imagine a set of six orthogonal axes, three for position and three for momentum, we could plot the individual state of one particle within the system. If we then multiply the number of axes by the number of particles N, we generate 6N total dimensions and could identify the system's microscopic state as a single point in what is called phase space. As time evolves, under the constraints of the system Hamiltonian H, the state moves through phase space tracing out a trajectory. Using phase space to plot s different systems, that all correspond to the same macroscopic state we arrive at what is conceptually illustrated in figure 3.1.1. Taking s large enough to approach a continuum of points we can write a conservation equation for the s systems in terms of a spatially and temporally dependent density.[51]

$$\frac{Df}{Dt} = \frac{\partial f^{(s)}}{\partial t} + \frac{\partial f^{(s)}}{\partial \vec{\mathbf{q}}_s} \cdot \frac{\partial \vec{\mathbf{q}}_s}{\partial t} + \frac{\partial f^{(s)}}{\partial \vec{\mathbf{p}}_s} \cdot \frac{\partial \vec{\mathbf{p}}_s}{\partial t} = 0 \qquad (3.1.3)$$

where $f^{(s)}$ is the density of s points, $\vec{\mathbf{q}}_s$ and $\vec{\mathbf{p}}_s$ are the position and momentum of all the particles and t is time.

With respect to time, each point in figure 3.1.1 translates through phase space tracing out a trajectory. If this system of particles is microcanonical the energy remains constant and we define a hyper-surface containing all the system states that correspond to that fixed amount of energy. The surface area of the hyper-surface could be used as an approximate measure of the number of states available to the system with all states considered equally likely. With an estimate for the number of states we calculate the system entropy using the Boltzmann relation

$$S = k_B \cdot \ln(\Omega) \tag{3.1.4}$$

where S is the entropy, k_B is Boltzmann's constant and Ω is the number of states. The temperature of the system is then determined using the thermodynamic definition

$$\frac{1}{T} = \left.\frac{\partial S}{\partial E}\right|_{N,V} \tag{3.1.5}$$

where T is temperature and E is the system's energy.

We now consider a classical three dimensional system of harmonic oscillators, similar to the system defined in the lattice dynamics section of the previous chapter. We write the system Hamiltonian H the following way

$$E = \mathrm{H}\{\vec{\mathbf{q}}_1 \ldots \vec{\mathbf{q}}_N, \vec{\mathbf{p}}_1 \ldots \vec{\mathbf{p}}_N\} = \sum_{i=1}^{N}\left(\frac{\vec{\mathbf{p}}_i^{\,2}}{2m_i} + \frac{1}{2}m_i \cdot \omega^2 \cdot \vec{\mathbf{q}}_i^{\,2}\right) \tag{3.1.6}$$

where $\vec{\mathbf{p}}_i$ is the particle momentum, $\vec{\mathbf{q}}_i$ is the displacement, m is the mass ω is the natural frequency forming the spring constant $K = m_i \cdot \omega^2$.

The number of states available to the system is then calculated by integrating over the coordinate space subject to the constraint that the energy be constant.

$$\Omega = \frac{1}{\hbar^{3N}} \cdot \int_{\substack{-\infty \\ \mathrm{H}=E}}^{\infty} d\vec{\mathbf{q}}_1 \ldots d\vec{\mathbf{q}}_N \cdot d\vec{\mathbf{p}}_1 \ldots d\vec{\mathbf{p}}_N \tag{3.1.7}$$

where $\hbar$ is similar to Planck's constant and is used to non-dimensionalize the integral. Out of convenience we make a canonical transformation that preserves phase space

$$\vec{\mathbf{q}}_i' \equiv \sqrt{m_i \cdot \omega} \cdot \vec{\mathbf{q}}_i \qquad \vec{\mathbf{p}}_i' \equiv \frac{\vec{\mathbf{p}}_i}{\sqrt{m_i \cdot \omega}}$$

where the energy is now

$$E = \frac{\omega}{2} \sum_{i=1}^{N} \left(\vec{\mathbf{p}}_i'^2 + \vec{\mathbf{q}}_i'^2 \right) \tag{3.1.8}$$

We then calculate the hyper-sphere radius as

$$R = \sqrt{\frac{2E}{\omega}} \tag{3.1.9}$$

and the integral to determine the number of states is now over $\vec{\mathbf{q}}_i'$ and $\vec{\mathbf{p}}_i'$ pairs

$$\Omega = \frac{1}{\hbar^{3N}} \cdot \int_{\substack{-\infty \\ \mathrm{H} \approx E}}^{\infty} d\vec{\mathbf{q}}'_1 \ldots d\vec{\mathbf{q}}'_N \cdot d\vec{\mathbf{p}}'_1 \ldots d\vec{\mathbf{p}}'_N \tag{3.1.10}$$

where we have relaxed the constant energy criterion to encompass energies close to E. We now approximate the integral with that of a thin volumetric shell, where

$$\Omega \approx \frac{2\pi^{3N}}{(3N-1)!} \cdot \left(\frac{2E}{\hbar\omega} \right)^{3N} \cdot \Delta R \tag{3.1.11}$$

Plugging this expression back into (3.1.4) yields an extensive expression for the entropy that we can differentiate, yielding an approximate expression for the energy in terms of the temperature.

$$\frac{\partial S}{\partial E} = \frac{1}{T} \approx k_B \cdot \left(\frac{3N}{E} \right) \tag{3.1.12}$$

$$E \approx N \cdot k_B \cdot T \tag{3.1.13}$$

Using this result we derive an expression for a single particle probability distribution as a function of its coordinates by integrating over all other coordinates in the system.

$$f(\vec{\mathbf{q}}_1, \vec{\mathbf{p}}_1) = \frac{\dfrac{1}{\hbar^{3N-1}} \cdot \displaystyle\int_{\substack{-\infty \\ \mathrm{H} \le E(N-1)}}^{\infty} d\vec{\mathbf{q}}_2 \ldots d\vec{\mathbf{q}}_N \cdot d\vec{\mathbf{p}}_2 \ldots d\vec{\mathbf{p}}_N}{\dfrac{1}{\hbar^{3N}} \cdot \displaystyle\int_{\substack{-\infty \\ \mathrm{H} \le E(N)}}^{\infty} d\vec{\mathbf{q}}_1 \ldots d\vec{\mathbf{q}}_N \cdot d\vec{\mathbf{p}}_1 \ldots d\vec{\mathbf{p}}_N} \tag{3.1.14}$$

After substituting the approximation of (3.1.11) this is reduced to

$$f(\vec{\mathbf{q}}_1,\vec{\mathbf{p}}_1)=\frac{\omega}{2\pi}\cdot\frac{N}{E}\cdot\left(1-\frac{\dfrac{\vec{\mathbf{p}}_1{}^2}{2\cdot m_1}+\dfrac{1}{2}m_1\cdot\omega^2\cdot\vec{\mathbf{q}}^2}{E}\right) \tag{3.1.15}$$

Since N is large a single particle only contributes a small portion of the total system energy allowing us to treat (3.1.15) as the first term of an exponential series, resulting in a properly normalized Gaussian distribution.

$$f(\vec{\mathbf{q}}_1,\vec{\mathbf{p}}_1)=\frac{\omega}{2\pi\cdot k_B\cdot T}\exp\left(\frac{-\left(\dfrac{\vec{\mathbf{p}}_1{}^2}{2\cdot m_1}\right)-\left(\dfrac{1}{2}m_1\cdot\omega^2\cdot\vec{\mathbf{q}}^2\right)}{E}\right) \tag{3.1.16}$$

Using the one particle distribution function we calculate the average kinetic and potential energies

$$\left\langle\frac{\vec{\mathbf{p}}_1{}^2}{2\cdot m_1}\right\rangle=\frac{3}{2}k_B\cdot T \qquad \left\langle\frac{1}{2}m_1\cdot\omega^2\cdot\vec{\mathbf{q}}^2\right\rangle=\frac{3}{2}k_B\cdot T \tag{3.1.17}$$

The result is commonly known as the equipartition theorem, because each quadratic term in the energy contributes $\frac{3}{2}k_B\cdot T$ to the total energy.

In modeling real crystals the potential energies are typically large and negative as compared to the smaller positive kinetic energy contributions. This has led to interesting questions concerning the appropriate definition of temperature in an MD simulation. However, here we adopt the following argument to justify our use of the first expression in (3.1.17) to calculate temperature in our simulations. Although the potential energy of empirical models is largely negative and heavily outweighs the kinetic energy contribution, the energy calculation could be adjusted to with an additive constant. This constant would cancel some of the lattice energy associated with the equilibrium state where the net forces are zero, but would not alter the system dynamics. The equilibrium state is the minimum energy configuration for the system and is analogous to that of the lattice dynamics system of oscillators described in chapter 2. The difference between these systems is that the total energy is zero in the oscillator case and corresponds to the lattice energy in real crystals. If we choose a constant to cancel the appropriate portion of lattice energy, and then perturb the atoms as in a classical MD simulation, we can achieve equipartition of kinetic and potential energy. In the energy fluctuations, changes in kinetic energy are compensated by potential energy generating equal magnitude with respect to the initial system energy. Since we may choose an appropriate constant to rescale our potential energy, equipartition should hold for an MD simulation in the microcanonical ensemble. We therefore calculate the temperature in a MD simulation as

$$T = \frac{1}{3N} \cdot \left\langle \frac{1}{2} m \cdot \vec{\mathbf{v}}^2 \right\rangle \tag{3.1.18}$$

In MD, a common approach is to approximate ensemble averages with times averages under the egodic hypothesis. In the remainder of this work we apply this assumption and approximate ensemble averaged quantities, denoted by $\langle \_ \rangle$, with time averages.

3.2 Green-Kubo Formula for Thermal Conductivity

With the phase space framework for connecting the microscopic picture of atomic motion to macroscopic variables we observe, we derive an expression for the thermal conductivity in terms of readily available quantities in a MD simulation. Here we briefly describe the approach developed by Green and Kubo based on the linearized Liouville equation. To proceed we recast (3.1.3) in terms of N particles recognizing that the second and third terms can be substituted in terms of the Hamiltonian equations of motion[20]

$$\frac{\partial f^{(N)}}{\partial t} = \left\{ \mathrm{H}, f^{(N)} \right\} \tag{3.2.1}$$

where the Poisson bracket $\{\_,\_\}$ is defined as

$$\{A, B\} \equiv \sum_{i=1}^{N} \left(\frac{\partial A}{\partial \vec{\mathbf{q}}_i} \cdot \frac{\partial B}{\partial \vec{\mathbf{p}}_i} - \frac{\partial A}{\partial \vec{\mathbf{p}}_i} \cdot \frac{\partial B}{\partial \vec{\mathbf{q}}_i} \right) \tag{3.2.2}$$

with A and B as arbitrary functions of the phase space variables. We then define the Liouville operator Γ as

$$\Gamma \equiv i \cdot \{ \mathrm{H}, \_ \}$$

so that

$$\frac{\partial f^{(N)}}{\partial t} = -i \cdot \Gamma f^{(N)} \tag{3.2.3}$$

where $i=\sqrt{-1}$.The assumption in linear response theory is that we can treat the Liouville operator as a function without explicit time dependence. Under that assumption we solve the Liouville equation for the time and phase space dependent density[20]

$$f^{(N)}(\vec{\mathrm{q}},\vec{\mathrm{p}},t)=\exp(-i\cdot t\cdot\Gamma)f^{(N)}(\vec{\mathrm{q}},\vec{\mathrm{p}},0) \tag{3.2.4}$$

Using this solution we derive an expression for thermal conductivity by considering the linear response to a thermal disturbance.

We momentarily step away from the microcanonical description of our system and consider a canonical system at equilibrium temperature T with a small temperature disturbance δT. By assuming that δT is stationary, its gradient is constant and that the system is in local equilibrium we can apply Boltzmann statistics and write the local probability distribution as

$$f_0=C\cdot\exp\left(-\frac{\varepsilon\cdot\Delta V}{k_B\cdot(T+\delta T)}\right)\approx C\cdot\exp\left(-\frac{\varepsilon\cdot\Delta V}{k_B\cdot T}\cdot\left(1-\frac{\delta T}{T}\right)\right) \tag{3.2.5}$$

where ε is the local energy density and ΔV is the local volume. Taking the second term in the exponent as the perturbation energy we write the perturbed Hamiltonian H' as

$$\mathrm{H}'(t)=-\int\varepsilon(\vec{\mathrm{q}}(t))\frac{\delta T(\vec{\mathrm{q}}(t))}{T}dV \qquad \mathrm{H}=\mathrm{H}_0+\mathrm{H}' \tag{3.2.6}$$

where H is the total energy and H_0 is the energy preceding the perturbation. Having now identified the perturbed system's Hamiltonian we rewrite the Liouville equation as

$$\frac{\partial f^{(N)}}{\partial t}=\left\{\mathrm{H}_0,f^{(N)}\right\}+\left\{\mathrm{H}',f_0^{(N)}\right\} \tag{3.2.7}$$

By substituting (3.2.6) into the second expression, we arrive at

$$\frac{\partial f^{(N)}}{\partial t}=-i\cdot\Gamma_0 f^{(N)}-\left(\frac{f_0^{(N)}}{k_B\cdot T^2}\right)\cdot\int\frac{\partial\varepsilon(\vec{\mathrm{q}}(t))}{\partial t}\cdot\delta T(\vec{\mathrm{q}}(t))dV \tag{3.2.8}$$

Using energy conservation

$$\frac{\partial\varepsilon}{\partial t}+\vec{\nabla}\cdot\vec{\mathrm{j}}_Q=0 \tag{3.2.9}$$

where ε is the local energy and $\vec{\mathrm{j}}_Q$ is the local heat flux, we then substitute into 3.2.8

$$\frac{\partial f^{(N)}}{\partial t}=-i\cdot\Gamma_0 f^{(N)}-\left(\frac{f_0^{(N)}}{k_B\cdot T^2}\right)\cdot\int\left[-\vec{\nabla}\cdot\left(\vec{\mathrm{j}}_Q(\vec{\mathrm{q}}(t))\cdot\delta T(\vec{\mathrm{q}}(t))\right)+\left(\vec{\mathrm{j}}_Q(\vec{\mathrm{q}}(t))\cdot\vec{\nabla}\cdot\delta T(\vec{\mathrm{q}}(t))\right)\right]dV$$

(3.2.10)

The first term in the integral is negligible allowing us to only integrate the second term, resulting in

$$\frac{\partial f^{(N)}}{\partial t} = -i \cdot \Gamma_0 f^{(N)} - \left(\frac{f_0^{(N)} \cdot V}{k_B \cdot T^2} \right) \cdot \vec{\nabla} \cdot \delta T \cdot \vec{\mathbf{J}}_Q \qquad (3.2.11)$$

where $\vec{\mathbf{J}}_Q$ is now the net heat flux in the system. We argue that the first term inside the integral of (3.2.10) is small assuming $\vec{\mathbf{j}}_Q(\vec{\mathbf{q}}(t))$ and $\delta T(\vec{\mathbf{q}}(t))$ are uncorrelated, resulting in a smaller the volumetric integral by comparison to the second term.

Based on this simplification we continue by solving (3.2.11) for the phase space density

$$f^{(N)}(\vec{\mathbf{q}},\vec{\mathbf{p}},t) = \frac{-V}{k_B \cdot T^2} \cdot \vec{\nabla} \cdot \delta T \cdot \int_{-\infty}^{t} \exp(-i \cdot (t-t') \cdot \Gamma_0) \vec{\mathbf{J}}_Q dt' \qquad (3.2.12)$$

and use it to calculate the ensemble averaged heat flux

$$\left\langle \vec{\mathbf{J}}_Q(t) \right\rangle = \iint \vec{\mathbf{J}}_Q(\vec{\mathbf{q}},\vec{\mathbf{p}},t) \cdot f^{(N)}(\vec{\mathbf{q}},\vec{\mathbf{p}},t) d\vec{\mathbf{q}} d\vec{\mathbf{p}} \qquad (3.2.13)$$

By substituting (3.2.12), we arrive at

$$\left\langle \vec{\mathbf{J}}_Q(t) \right\rangle = \frac{-V}{k_B \cdot T^2} \int_{-\infty}^{t} \left\langle J_{Qx}(t) \cdot \vec{\mathbf{J}}_Q(t-t') \right\rangle \cdot \vec{\nabla} \cdot \delta T \cdot dt \qquad (3.2.14)$$

We then extract the temperature gradient, since we assumed it to be time independent resulting in an expression for the heat flux, similar to Fourier's law. We now identify an expression for thermal conductivity, using a Fourier transform to rewrite the integral.

$$\kappa_{ij}(T,\omega) = \frac{V}{k_B \cdot T^2} \int_{0}^{\infty} \left\langle J_{Qi}(0) \cdot J_{Qj}(\tau) \right\rangle \cdot \exp(-i\omega \cdot \tau) \cdot d\tau \qquad (3.2.14)$$

$\kappa_{ij}(T,\omega)$ is the temperature and frequency dependent thermal conductivity tensor, where ω is the perturbation frequency and the ij subscripts denote tensor components. In macroscopic heat conduction we most often encounter constant fluxes and need the zero frequency limit of (3.2.14)[20]

$$k(T) = \frac{V}{3 \cdot k_B \cdot T^2} \int_{0}^{\infty} \left\langle \vec{\mathbf{J}}_Q(0) \cdot \vec{\mathbf{J}}_Q(\tau) \right\rangle \cdot d\tau \qquad (3.2.15)$$

$\kappa(T)$ is the thermal conductivity used in macroscopic problems, where the time scale of system perturbations are orders of magnitude slower than atomic scale fluctuations. However for high frequency inputs of similar time scale as the atomic fluctuations, the frequency dependent thermal conductivity can deviate from the static value by orders of magnitude.[12]

We are now left with the task of determining the volume integrated heat flux for the system in terms of the microscopic variables we can extract from an MD simulation. To do this we revert back to (3.2.9) and develop a quantum mechanical heat flux operator that is generalized for any phase of matter and can be applied to any empirical form of potential energy.[52] Here we recast (3.2.9) as

$$\dot{\mathrm{H}}(\mathbf{x}) + \vec{\nabla} \cdot \mathbf{s}(\mathbf{x}) = 0 \tag{3.2.16}$$

where $\mathbf{s}(\mathbf{x})$ is now a local heat flux operator. $\dot{\mathrm{H}}(\mathbf{x})$ is related to the energy density operator and H by

$$\dot{\mathrm{H}}(\mathbf{x}) = \frac{1}{i \cdot \hbar}\{\mathrm{H}(\mathbf{x}), \mathrm{H}\} \tag{3.2.17}$$

where i is imaginary in the forthcoming steps when not used as a labeling subscript and $\hbar$ is Planck's constant divided by 2π. Combining these expressions gives,

$$\vec{\nabla}\mathbf{s}(\mathbf{x}) = \frac{i}{\hbar}\{\mathrm{H}(\mathbf{x}), \mathrm{H}\} \tag{3.2.18}$$

and a generic form for the Hamiltonian operator is assumed in order to express the heat flux operator in terms of microscopic variables.

$$\mathrm{H} = \sum_{i=1}^{N}\left(\frac{\vec{\mathbf{p}}_i^{\,2}}{2 \cdot m_i} + \Phi_i\right) \tag{3.2.19}$$

We then define a local energy density operator in terms of a spatially dependent weighting function that incorporates contributions to the heat flux from the local environment.[52]

$$\mathrm{H}(\mathbf{x}) = \frac{1}{2}\sum_{i=1}^{N}\left\{\Delta(\mathbf{x} - \vec{\mathbf{q}}_i)\left(\frac{\vec{\mathbf{p}}_i^{\,2}}{2 \cdot m_i} + \Phi_i\right) + H.c.\right\} \tag{3.2.20}$$

where *H.c.* is the Hermitian conjugate and $\Delta(\mathbf{x} - \vec{\mathbf{q}}_i)$ is a spatial weighting function normalized to unity.

$$\int \Delta(\mathbf{x}-\vec{\mathbf{q}}_i)dV = 1 \tag{3.2.21}$$

Taking

$$\Delta(\mathbf{x}-\vec{\mathbf{q}}_i)=\left(\frac{1}{l\cdot\sqrt{\pi}}\right)^3\cdot\exp\left(-\left(\frac{|\mathbf{x}-\vec{\mathbf{q}}_i|}{l}\right)^2\right), \tag{3.2.22}$$

using the commutation relations of the position and momentum operators and Taylor expanding the spatial weighting function allows simplification of (3.2.18) to

$$\frac{i}{\hbar}\{\mathrm{H}(\mathbf{x}),\mathrm{H}\}=\sum_{\alpha}\frac{\partial \mathbf{s}_{\alpha}}{\partial \mathbf{x}_{\alpha}} \tag{3.2.23}$$

Here α denotes a vector component and the spatially dependent heat flux is given by

$$\mathbf{s}(\mathbf{x})=\frac{1}{2V}\left[\sum_{i=1}^{N}\left(\Delta(\mathbf{x}-\vec{\mathbf{q}}_i)\frac{\mathbf{p}_i}{2m_i}+\frac{\mathbf{p}_i}{2m_i}\Delta(\mathbf{x}-\vec{\mathbf{q}}_i)\right)\left(\frac{\vec{\mathbf{p}}_i^{\,2}}{2\cdot m_i}+\Phi_i\right)+\ldots\right.$$

$$\left.\sum_{ij}^{N}\left(\left(1+\frac{1}{2!}\sum_{b}(\mathbf{q}_i^{\,b}-\mathbf{q}_j^{\,b})\frac{\partial}{\partial \mathbf{x}^b}+\ldots\right)\Delta(\mathbf{x}-\vec{\mathbf{q}}_i)\right)\times(\vec{\mathbf{q}}_i-\vec{\mathbf{q}}_j)\cdot\frac{1}{i\hbar}\left\{\frac{\vec{\mathbf{p}}_i^{\,2}}{2\cdot m_i},\Phi_i\right\}\right]+H.c. \tag{3.2.24}$$

We now spatially average the local heat flux operator, to yield an expression suitable for implementation in a MD simulation.[52]

$$\mathbf{s}=\frac{1}{V}\sum_{i=1}^{N}\left[\left(\frac{\vec{\mathbf{p}}_i^{\,2}}{2\cdot m_i}+\Phi_i\right)\cdot\frac{\vec{\mathbf{p}}_i}{m_i}+\sum_{\substack{j=1\\ j\neq i}}^{N}\left(\frac{\partial\Phi_j}{\partial\vec{\mathbf{q}}_i}\cdot\frac{\vec{\mathbf{p}}_i}{m_i}\right)\cdot(\vec{\mathbf{q}}_i-\vec{\mathbf{q}}_j)\right] \tag{3.2.25}$$

This expression has two physically meaningful terms that correspond to the two mechanisms that carry heat in all phases of matter. The first term, often called the convective or diffusion term, dominates in liquids and gases where energy is transported via constituent molecules. In solids the second term dominates because the forces are large and atoms do not diffuse through the crystal.

One subtle aspect of this derivation that has been overlooked in other studies is the summation sequence and appropriate derivative in the second term. In words, the summation is over all interactions and the derivative is how an atom i changes the potential energy of a neighboring atom j. When multiplied by its own velocity, it represents the power transmitted from each atom to its environment, or the energy divergence rate. Therefore it is necessary that the summation in (3.2.25) be carried out over all atomic interactions in the system without pre-factors to cancel over counting. In a pair potential this corresponds to the entire force between atoms, however in a three body potential only particular contributions should be included in (3.2.25).

With this framework we use the ergodic hypothesis[27] to approximate the ensemble averaged heat flux autocorrelation in (3.2.15) with the time average. Our results support that this assumption is reasonable, as we use this formulation to calculate to thermal conductivity from a MD simulation. Although the Green-Kubo method has shown excellent agreement with experimental results, it is still unclear what the underlying heat conduction mechanisms are. To illuminate the mechanisms of thermal transport we seek another formalism that can describe thermal conductivity in terms of phonons and their mean free path. In chapter 1 we used kinetic theory as an analogous argument to draw a parallel between molecules and phonons. Here we perform a more rigorous derivation of the same expression, starting from the Liouville equation and eventually taking an analogous perspective of phonons in phase space as opposed to molecules.

3.3 Boltzmann Transport Equation Approach for Thermal Conductivity

We begin this section by first deriving the Boltzmann equation for gas molecules.[51] We then proceed to discuss the relaxation time approximation and derive an expression for heat conduction based on phonon transport. This expression has similar form to Fourier's law and yields an expression for thermal conductivity that involves the properties of phonons. The resulting expression allows us to calculate the spectral contributions to thermal conductivity, allowing us to draw conclusions about the dominating thermal transport mechanisms. We start by recasting the Liouville equation considering a system of particles that are broken into two regions. A joint system Hamiltonian is then composed of two regional Hamiltonians and an interaction Hamiltonian as follows

$$\mathrm{H} = \mathrm{H}_s + \mathrm{H}_{N-s} + \mathrm{H}' \tag{3.3.1}$$

where the subscript N denotes the total number of particles and s denotes the particles in the system of interest, as they interact with particles not contained in the group $N-s$. We assume the Hamiltonian has the following form

$$\mathrm{H}_s = \sum_{n=1}^{s}\left[\left(\frac{\vec{\mathbf{p}}_n^{\,2}}{2m}\right)+U(\vec{\mathbf{q}}_n)+\frac{1}{2}\cdot\sum_{\substack{m=1\\ m\neq n}}^{s}\Phi(\vec{\mathbf{q}}_n-\vec{\mathbf{q}}_m)\right]$$

$$\mathrm{H}_{N-s} = \sum_{i=s+1}^{N}\left[\left(\frac{\vec{\mathbf{p}}_i^{\,2}}{2m}\right)+U(\vec{\mathbf{q}}_i)+\frac{1}{2}\cdot\sum_{\substack{j=s+1\\ j\neq i}}^{N}\Phi(\vec{\mathbf{q}}_i-\vec{\mathbf{q}}_j)\right] \tag{3.3.2}$$

with external potential $U(\vec{\mathbf{q}})$ and a particle interaction potential Φ. The interaction Hamiltonian H' is then

$$\mathrm{H}' = \sum_{n=1}^{s}\sum_{i=s+1}^{N}\Phi(\vec{\mathbf{q}}_n-\vec{\mathbf{q}}_i) \tag{3.3.3}$$

We rewrite the phase space density in terms of a normalized probability distribution function ρ_s based on the coordinates in the group s

$$f_s(\vec{\mathbf{q}}_1,\ldots,\vec{\mathbf{p}}_s,t)=\frac{N!}{(N-s)!}\int\prod_{i=s+1}^{N}dV_i\rho(\vec{\mathbf{q}},\vec{\mathbf{p}},t)=\frac{N!}{(N-s)!}\rho_s(\vec{\mathbf{q}}_1,\ldots,\vec{\mathbf{p}}_s,t) \tag{3.3.4}$$

The time evolution of the distribution is then

$$\frac{\partial\rho_s}{\partial t}=\int\prod_{i=s+1}^{N}dV_i\frac{\partial\rho}{\partial t}=\int\prod_{i=s+1}^{N}dV_i\{\rho,\mathrm{H}_s+\mathrm{H}_{N-s}+\mathrm{H}'\} \tag{3.3.5}$$

This involves three separate terms in the Poisson bracket, which are evaluated separately. Using integration by parts the second term goes to zero and the first and last term are written as

$$\int\prod_{i=s+1}^{N}dV_i\{\rho,\mathrm{H}_s\}=\left\{\int\prod_{i=s+1}^{N}dV_i\rho,\mathrm{H}_s\right\}=\{\rho_s,\mathrm{H}_s\} \tag{3.3.6}$$

$$\int\prod_{i=s+1}^{N}dV_i\left[\sum_{n=1}^{s}\frac{\partial\rho}{\partial\vec{\mathbf{p}}_n}\cdot\sum_{j=s+1}^{N}\frac{\partial\Phi(\vec{\mathbf{q}}_n-\vec{\mathbf{q}}_j)}{\partial\vec{\mathbf{q}}_n}+\sum_{j=s+1}^{N}\frac{\partial\rho}{\partial\vec{\mathbf{p}}_n}\cdot\sum_{n=1}^{s}\frac{\partial\Phi(\vec{\mathbf{q}}_j-\vec{\mathbf{q}}_n)}{\partial\vec{\mathbf{q}}_j}\right] \tag{3.3.7}$$

The integral in (3.3.6) involves the sum of $N-s$ versions of the same integral and can be simplified to the following in terms of the phase space densities[51]

$$\frac{\partial f_s}{\partial t}+\{\mathrm{H}_s,f_s\}=\sum_{n=1}^{s}\int dV_{s+1}\frac{\partial\Phi(\vec{\mathbf{q}}_n-\vec{\mathbf{q}}_{s+1})}{\partial\vec{\mathbf{q}}_n}\cdot\frac{\partial f_{s+1}}{\partial\vec{\mathbf{p}}_n} \tag{3.3.9}$$

When written in the limit that s goes to unity, (3.3.9) is called the Boltzmann equation, which describes the time evolution of a phase space density or probability distribution with two terms. In the absence of interactions the equation reduces to the left hand side, called the streaming terms, since the phase space density evolution becomes identical to that of an incompressible fluid. The right hand side is called the collision term and governs the rate at which particle interactions take place.

We now change our interpretation of the Boltzmann equation from that of gas molecules to phonons, as we seek an approximation for the collision integral in order to solve. Here we adopt the relaxation time approximation, whereby we model the collision integral as follows[20]

$$\left(\frac{\partial f}{\partial t}\right)_C = -\frac{f - f_0(E,T)}{\tau(\vec{\mathbf{q}},\vec{\mathbf{k}})} \tag{3.3.10}$$

where $\left(\frac{\partial f}{\partial t}\right)_C$ is the right hand side of (3.3.9), f_0 is the equilibrium distribution and $\tau(\vec{\mathbf{q}},\vec{\mathbf{k}})$ is the relaxation time. The relaxation time approximation assumes that when the system is perturbed it decays exponentially back to the equilibrium distribution, seen by solving

$$f - f_0 = C\exp\left(-\frac{t}{\tau}\right) \tag{3.3.11}$$

This is a useful approximation for the collision integral as we validate the assumption for phonons via the following argument.

In chapter 1 we established an analogy between lattice wave attenuation and phonon scattering and henceforth acknowledge a wave-particle duality for thermal energy transport. Under this context, attenuating lattice waves are usually modeled with a decaying exponential, since modes are initially excited and absorbed by atoms while propagating. The decay rate varies for differing phonons, however we take the relaxation time to be constant for phonons of a particular wave vector and polarization. In the particle picture the decay rate corresponds to the scattering rate for phonons of a particular wave vector and polarization. We justify the single mode relaxation time approximation through its dual contextual interpretation as attenuating lattice waves, which are known to decay exponentially in the audible regime.

Recasting the Boltzmann equation with the single mode relaxation time (SMRT) approximation it is now possible to solve the phonon Boltzmann equation and derive an expression for thermal conductivity.[20]

$$\frac{\partial f}{\partial t} + \vec{\mathbf{v}} \cdot \vec{\nabla}_{\vec{\mathbf{q}}} f + \frac{\vec{\mathbf{F}}}{m} \cdot \vec{\nabla}_{\vec{\mathbf{v}}} f = -\frac{f - f_0(E,T)}{\tau(\vec{\mathbf{q}},\vec{\mathbf{k}})} \tag{3.3.12}$$

This is a generalized expression for particles, where $\vec{\mathbf{v}}$ is velocity and $\frac{\vec{\mathbf{F}}}{m}$ is the acceleration and the symbols $\vec{\nabla}_{\vec{\mathbf{q}}}$, $\vec{\nabla}_{\vec{\mathbf{v}}}$ denote gradients with respect to position and velocity respectively. Next we write (3.3.12) in terms of the deviation from equilibrium statistics, where $g = f - f_0$

$$\frac{\partial g}{\partial t} + \frac{\partial f_0}{\partial t} + \vec{\mathbf{v}} \cdot \vec{\nabla}_{\vec{\mathbf{q}}} g + \vec{\mathbf{v}} \cdot \vec{\nabla}_{\vec{\mathbf{q}}} f_0 + \frac{F}{m} \cdot \vec{\nabla}_{\vec{\mathbf{v}}} f_0 + \frac{F}{m} \cdot \vec{\nabla}_{\vec{\mathbf{v}}} g = -\frac{g}{\tau} \tag{3.3.13}$$

and

$$f = f_0 - \tau \cdot \left(\vec{\mathbf{v}} \cdot \vec{\nabla}_{\vec{\mathbf{q}}} f\right) \tag{3.3.14}$$

We arrive at (3.3.14) by first assuming that g is small and therefore its derivatives can be neglected. We also note that phonons come from the lattice wave solution (2.4.2) and therefore do not accelerate. In addition we treat phonons as non-interacting bosons and apply Bose-Einstein statistics

$$f_0 = \frac{1}{\exp\left(\frac{\hbar\omega}{k_B T}\right) - 1} \tag{3.3.15}$$

where ω is the phonon frequency, carrying energy $\hbar\omega$. With respect to the spatial gradient in the Boltzmann equation, the equilibrium distribution achieves spatial dependence through the temperature field resulting in

$$f(q,k) = f_0 - \tau \cdot \left(\vec{\mathbf{v}} \cdot \frac{df_0}{dT} \cdot \vec{\nabla} T\right) \tag{3.3.16}$$

If we take a one dimensional heat flow example, the heat flux can be written as a sum over allowable phonon states, where we write the energy flux in the x direction as

$$J_{Qx}(x) = \frac{1}{V} \cdot \sum_{\nu} \sum_{\vec{\mathbf{k}}_{\min}}^{\vec{\mathbf{k}}_{\max}} \hbar\omega \cdot f \cdot v_x \tag{3.3.17}$$

where $J_{Qx}(x)$ is the component of heat flux in the x direction, V is volume, v denotes the sum over all polarizations and the vectors $\vec{\mathbf{k}}_{\max}$ and $\vec{\mathbf{k}}_{\min}$ are limited by the Brillouin zone and crystal boundary respectively. For large crystals we convert the summation to an integral by dividing out the differential spacing $dk_{\alpha} = \left(\frac{2\pi}{L}\right)$

$$J_{Qx}(x) = \frac{1}{V} \cdot \sum_{v} \iiint \hbar\omega \cdot f \cdot v_x \cdot \frac{dk_x dk_y dk_z}{\left(\frac{2\pi}{L}\right)^3} \tag{3.3.18}$$

We then convert the integral over wave vectors to an integral over frequency and two polar integrals

$$J_{Qx}(x) = \sum_{v} \int_{0}^{\omega_{\max}} \int_{0}^{2\pi} \int_{0}^{\pi} \hbar\omega \cdot f \cdot v \cdot \cos(\theta) \cdot \left(\frac{D(\omega)}{4\pi}\right) \cdot \sin(\theta) d\theta d\phi d\omega \tag{3.3.19}$$

where the x component of v is the product $v \cdot \cos(\theta)$ and $\sin(\theta) d\theta d\phi$ is what remains of the solid angle where k^2 has been absorbed into $\frac{D(\omega)}{4\pi}$, the density of states per unit solid angle.

It is important to divert our attention here and consider the density of states in detail as a reasonable approximation can be calculated using lattice dynamics. Using the concept of a Brillouin zone we developed in chapter 2, we invert the crystal lattice such that it is viewed in an isotropic reciprocal space whereby all the lattice sites are referenced by reciprocal lattice $\vec{\mathbf{k}}$ vectors with units of inverse distance. By representing the reciprocal lattice graphically in $\vec{\mathbf{k}}$-space, we can find the number of wave vectors contained within a spherical shell of radius $\left\|\vec{\mathbf{k}}\right\|$. Our approximation is based on the number of reciprocal lattice points contained within the shell, which is equal to the volume of the shell divided by the volume occupied by each state in $\vec{\mathbf{k}}$-space.

$$D\left(\left\|\vec{\mathbf{k}}\right\|\right) = \frac{4\pi \cdot k^2 dk}{\left(\frac{2\pi}{L}\right)^3} \tag{3.3.20}$$

This is often called the density of states or DoS. The density of states represents the number of terms from the original summation in (3.3.17) that would occur in the interval

$d\vec{k}$. The units of DoS in (3.3.19) are number of states per unit volume, per unit wave vector or frequency, which is a straightforward conversion from (3.3.20).

Equation (3.3.19) can be written in different ways, however we used a frequency interval form because it is a function we can numerically determine using lattice dynamics. A typical DoS approximation involves assuming the dispersion is linear and substituting into (3.3.20) to get a parabolic function of frequency. Although this approximation can give reasonable values for thermal conductivity it is only valid for low frequencies where phonons travel at sound velocities. In this study we consider the full frequency content of the density of states, by first choosing an appropriately partitioned grid of Brillouin zone points. We then calculate the dispersion curves along those directions and count how many frequencies fall within a particular interval. This methodology provides an isotropic picture of the DoS, a noted assumption in our thermal conductivity calculation.

Returning to the thermal conductivity derivation, we substitute (3.3.16) into (3.3.19) and add $\cos(\theta)$ for the appropriate velocity component in the nonequilibrium distribution f.

$$J_{Qx}(x) = \sum_{\nu} \int_{0}^{\omega_{\max}} \int_{0}^{2\pi}\int_{0}^{\pi} \hbar\omega \cdot \left(f_0 - \tau \cdot \left(\vec{v} \cdot \frac{df_0}{dT} \cdot \vec{\nabla} T \right) \right) \cdot v \cdot \cos(\theta) \cdot \left(\frac{D(\omega)}{4\pi} \right) \cdot \sin(\theta) d\theta d\phi d\omega \tag{3.3.21}$$

We then integrate over the polar angles and extract the temperature gradient, noticing that the first term goes to zero, leaving

$$J_{Qx}(x) = -\left[\frac{1}{3} \cdot \sum_{\nu} \int_{0}^{\omega_{\max}} \hbar\omega \cdot \frac{df_0}{dT} \cdot v^2 \cdot \tau \cdot D(\omega) \cdot d\omega \right] \cdot \vec{\nabla} T \tag{3.3.22}$$

This expression resembles Fourier's law and identifies the thermal conductivity as[20]

$$\kappa(T) = \frac{1}{3} \cdot \int_{0}^{\omega_{\max}} C(\omega) \cdot v^2(\omega) \cdot \tau(\omega) \cdot d\omega \tag{3.3.23}$$

This expression has the same components as the kinetic theory expression, derived in chapter 1, with the important difference being the frequency dependent integral. Using lattice dynamics we can determine the specific heat and group velocity in the thermal conductivity integral (3.3.23), but are left with the task of determining the phonon relaxation time.

3.4 Normal Mode Coordinates and Relaxation Time

In the lattice dynamics section of chapter 2, we showed that the solution to the eigenvalue equation produced eigenvectors that corresponded to the phonon polarizations. In that model we can fully expand the atomic displacements in terms of a Fourier series of normal modes, as a superposition of plane waves. The atoms in a solid crystal structure are then fully described by the allowable normal modes where an individual atomic displacement is written as[50]

$$\vec{\mathbf{u}}(jl,t) = \frac{1}{\left(Nm_j\right)^{\frac{1}{2}}} \cdot \sum_{\vec{\mathbf{k}},\nu} \vec{\mathbf{e}}\left(j,\vec{\mathbf{k}},\nu\right) \cdot \exp\left(i\vec{\mathbf{k}} \cdot \vec{\mathbf{r}}(jl)\right) \cdot Q\left(\vec{\mathbf{k}},\nu\right) \tag{3.4.1}$$

$\vec{\mathbf{u}}(jl,t)$ is the displacement of an atom labeled j in unit cell l with mass m, $\vec{\mathbf{e}}\left(j,\vec{\mathbf{k}},\nu\right)$ is the mode eigenvector, $\vec{\mathbf{k}}$ is the wave vector, $\vec{\mathbf{r}}(jl)$ is the lattice site position and the time dependent amplitude of the mode is $Q\left(\vec{\mathbf{k}},\nu\right)$ where ν denotes polarization. This is an inverse Fourier decomposition of the atomic displacements where the original transform can be computed as

$$Q\left(\vec{\mathbf{k}},\nu\right) = \left(\frac{m_j}{N}\right)^{\frac{1}{2}} \cdot \sum_{j,l} \vec{\mathbf{e}}^*\left(j,\vec{\mathbf{k}},\nu\right) \cdot \vec{\mathbf{u}}(jl,t) \cdot \exp\left(-i\vec{\mathbf{k}} \cdot \vec{\mathbf{r}}(jl)\right) \tag{3.4.2}$$

where the * superscript implies the complex conjugate of $\vec{\mathbf{e}}\left(j,\vec{\mathbf{k}},\nu\right)$ as $Q\left(\vec{\mathbf{k}},\nu\right)$ is also a generally complex quantity, although the actual atomic displacements are real values.

We now apply the model from our previous discussion of the relaxation time, whereby we treat the normal lattice mode attenuation as a decaying function due to the anharmonic components of the interatomic potential. Under this approximation we write the normal mode displacement in terms of two temperature dependent quantities called the phonon frequency shift and line width.[53]

$$Q\left(\vec{\mathbf{k}},\nu,t\right) = Q_0 \cdot \exp\left(-i(\omega + \Delta - i\mu) \cdot t\right) \tag{3.4.3}$$

The frequency shift Δ is caused by the softening of spring constants when bonds are stretched under finite temperature interactions. The line width μ captures the decaying effect of attenuation. As temperature increases, energy is extracted from lattice waves at a faster rate and contributes to the excitation of additional waves. In the particle perspective, these phenomena correspond to phonon creation and annihilation. Using this type of model we establish connections between phonons, lattice normal modes and the atomic displacements which we simulate using MD.

To extract the phonon relaxation time we are essentially interested in the attenuation decay time, which we extract by first using (3.4.2) to calculate the normal mode amplitudes within our simulation domain. We then calculate relaxation time from the autocorrelation function of the normal mode's temporal deviation from average. From the autocorrelation function for a particular mode we calculate its time constant, as it decays exponentially, assuming (3.4.3) is an accurate description. We expect the autocorrelation to decay because of the nonlinear effects in the potential, causing the mode amplitude to be non periodic. The extracted time constant is then the single mode relaxation time[28,53]

$$\tau(\vec{\mathbf{k}},\nu)=\frac{\int_0^\infty \left\langle \delta Q(\vec{\mathbf{k}},\nu,t)\cdot \delta Q(\vec{\mathbf{k}},\nu,0)\right\rangle}{\left\langle \delta Q^2(\vec{\mathbf{k}},\nu,0)\right\rangle} \tag{3.4.4}$$

where δQ implies the deviation from the time averaged value.

This now completes our analytical framework and we proceed by simulating diamond-structured silicon using EDIP. We use the framework outlined in the chapter to calculate thermal conductivity using Green-Kubo relations and also extract frequencies and relaxation times of different modes within the simulation domain. These tools enable us to consider the frequency and direction dependence of the relaxation times to check the validity of the isotropic assumption. Once the relaxation times are calculated, we generate a full spectral view through interpolation and combine the results with our calculation of the frequency dependent specific heat and group velocity. The three components will allow us to numerically integrate (3.3.23) and determine the spectral contributions to thermal conductivity.

Chapter 4: Simulation Procedures

In the preceding chapters we introduced the concept of MD simulations and discussed the tools needed to analyze the trajectory and determine thermal properties. Here we outline the procedure and details of our investigation, which consisted of 250 independent MD simulations. In our research, we set out to resolve the phonon mean free path and dominant heat conduction mechanism in bulk silicon. In this chapter we present the essential details needed to reproduce our results. We start with our choice of iteration timestep and then discuss the computational resources that were used. We then address issues related to our Green-Kubo calculations and the convergence of the heat flux autocorrelation function. Lastly we give the details of our simulations used to calculate the phonon relaxation time and outline our methodology for generating the full spectral view of the contributions to thermal transport.

4.1 Choosing a Suitable Timestep

In general writing a MD program is rather straightforward in its structure, however most of the time is spent in the debugging stage searching for errors. Since it is of no consequence to our results, we will not go into detail of the MD programming structure, but will consider our method for choosing a suitable timestep. All of our simulations were conducted in three dimensions using equilibrium MD with periodic boundary conditions. We were able to check for trajectory related programming errors by comparing our force calculation with that of a subroutine written by the author of the potential.[54] Other types of coding errors were discovered through monitoring the deviations in total energy, since errors tend to make the system unstable.

Typical MD timesteps are on the order of femtoseconds while simulation times are on the order of nanoseconds, consisting of millions of timesteps. Although it may appear trivial, an acceptable factor of two increase in timestep decreases the simulation time by half. For our runs, which took more than one day, the difference between waiting one day as opposed to two can significantly increase the efficiency of the program development phase. If the selected timestep is too large, errors aggregate in the trajectory and the simulation cannot accurately reflect the dynamics contained in the potential. This level of error is unavoidable when using finite timestep algorithms, since an inherent amount of numerical error is inevitable when approximating the solution to Newton's equations.

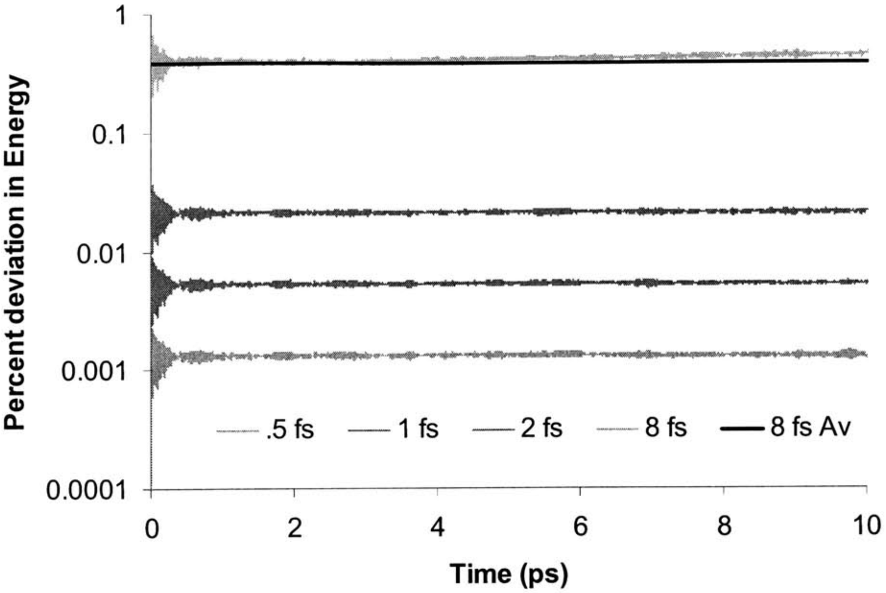

Figure 4.1 Percent deviation in energy per atom for different size timesteps

Figure 4.1 shows deviations in energy for different MD timesteps in a simulation of 4x4x4 unit cells at 1000K, where we chose 1 femtosecond for the subsequent production runs. The figure shows that a timestep of 8 femtoseconds is too large as the energy deviation steadily increases with time. The choice of timestep is somewhat qualitative, since there is no rigid criterion for its selection. It is difficult to determine when a timestep is sufficiently small, as it may preserve the energy but may also inaccurately represent vibrational dynamics. We chose 1 femtosecond based on the highest frequency vibrations we expect in our simulations. In our lattice dynamics calculation the highest phonon frequency is bounded by roughly 20THz, corresponding to one oscillation every 50 femtoseconds. A timestep of 1 femtosecond allows us to break up the fastest fluctuations into 50 sampled points. A factor of two larger timestep may also be justifiable, however to maximize reliability in our results we used 1 femtosecond for all the production runs.

4.2 Simulation Details

Our simulations were written in Fortran 90 and executed on a 25-node Dell Linux cluster. The cluster was donated by Intel corporation and has a front end node with dual 3.6 GHz Xeon processors 1MB cache, accompanied by 8Gb of RAM. The simulations were run on the 24 computing nodes, with dual 3.0 GHz Xeon processors 2MB cache and 4Gb of RAM. All our simulations were run using serial codes without any parallel processing or communication.

In this study our particular interest involves atomic vibration, where we study attenuating lattice waves in a silicon crystal to determine their relaxation rate. As a result we focused our simulations in the temperature range between 300K and 1000K, where we expected to see strong temperature dependence for thermal conductivity. In this regime we chose eight temperatures evenly spaced by 100K. The two remaining temperatures were 350K and 450K, chosen toward the lower temperatures where umklapp scattering changes more steeply with temperature.

All analysis methods introduced in chapter 3 involve the ergodic approximation, where we compensate phase space sampling with long time simulations. To decrease the error due to this assumption we repeated simulations five times with independently randomized initial conditions at each temperature. The results for the five simulations were then averaged together with the standard deviations treated as error.

In preliminary runs we found negligible differences when changing the lattice parameter to allow for thermal expansion and therefore decided to keep it constant at the room temperature experimental value of 5.4309 Å.[55] At high temperatures this introduces additional pressure due to the necessity for thermal expansion, however we did not observe significant impact on our results, because the thermal properties of solids are typically pressure independent. In our study we conducted simulations that fell into two categories, Green-Kubo calculations and relaxation time calculations. Each type of simulation had different requirements, outlined in the following sections.

4.3 Green-Kubo Simulations

For the Green-Kubo calculation of thermal conductivity we track the volume averaged heat flux and calculate its autocorrelation function. The heat flux autocorrelation is a time correlation function that is integrated, in accordance with (3.2.15), to determine thermal conductivity at the simulated temperature. Time correlations measure the ability of two functions to represent each other in the same way Fourier coefficients measure the correspondence between a function and a series of sines or cosines. In a time autocorrelation, a function is compared to itself at later times to measure orthogonality with increasing time separation Δt as follows

$$A_{AC}(\Delta t) = \frac{1}{t_2 - t_1} \int_{t_1}^{t_2} A(t) \cdot A(t + \Delta t) dt \qquad (4.3.1)$$

where $A_{AC}(\Delta t)$ is the autocorrelation function of quantity $A(t)$ on the interval $t_2 - t_1$. Numerical evaluation of (4.3.1) involves computation of average inner product values executed on a sampling interval $t_2 - t_1$. One concern was quantifying the necessary sampling time for the heat flux autocorrelation function (HFAC) to converge to the infinite value. In the following figures we show preliminary results of the HFAC integral.

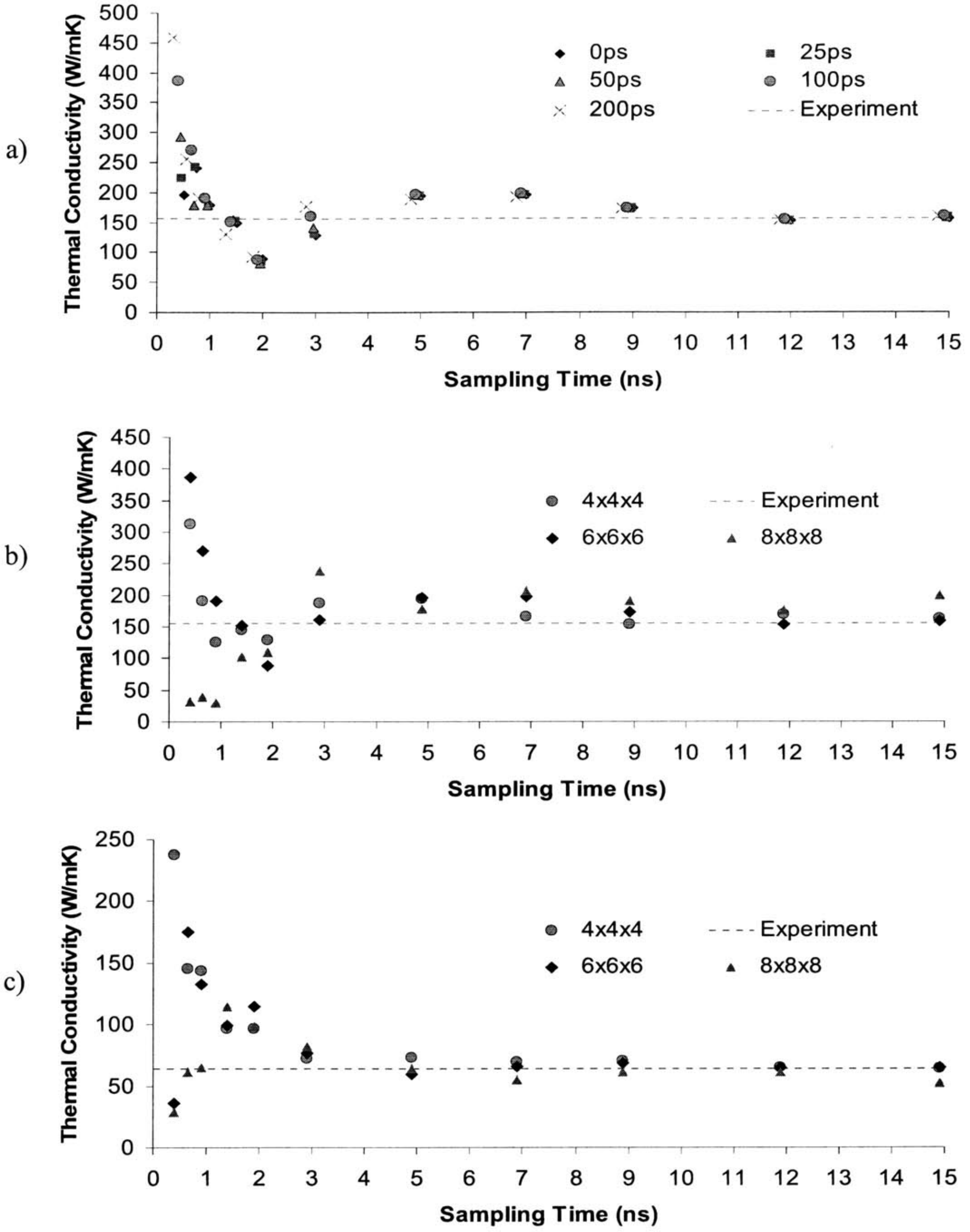

Figure 4.3.1 HFAC convergence in Green-Kubo Thermal Conductivity Calculation: (a) 300K Integral dependence on equilibration time and sampling time, (b) 300K Integral dependence on system size and sampling time, (c) 600K Integral dependence on system size and sampling time

Figure 4.3.1 shows that the thermal conductivity integral changes with longer sampling times. Although energy is conserved throughout the simulation we allowed for varying amounts of initializing equilibration time, since the system is initialized from a highly improbable state. All simulations were started with atoms positioned at their lattice site and random velocities corresponding to the desired temperature. The initial state has low entropy and is highly improbable at equilibrium, as the system needs some time to maximize its entropy. We therefore tested the effects of the equilibration time and found that 100 picoseconds was sufficient time for the system to lose memory of its initial configuration, shown in figure 4.3.1 (a).

Figure 4.3.1 (b) shows that for short sampling times the HFAC is incomplete and does not fully decay leading to under approximated integral values. The integral then increases to roughly two or three times the converged value, because the function decays but is generally larger than the converged function with the same shape. Figure 4.3.1 b and c show this trend differed for the larger 8x8x8 system. We initially expected the convergence rate to increase with system size, however at longer times the results show similar trends for all three systems. Beyond five nanoseconds the function begins converging and we selected ten nanoseconds as a suitable simulation length for our study. We were unable to determine if there is a physical mechanism that governs the amount of time it takes to converge. As shown in the figure, we also observed similar results systems with differing size. In these preliminary runs a slight temperature dependent effect was observed, shown in figure 4.3.1 (c), which may be due to the faster decay of HFAC functions at higher temperatures.

We also observed that the sampling method could also change the results. In calculating a time-averaged autocorrelation, the function's values depend on the time separation between points of an inner product. Although 3.2.15 is an infinite integral, the functions at all temperatures decayed within the first 150 picoseconds, after which small random oscillations occurred with insignificant impact on the results. The data after that point was subsequently neglected, while function values were generated by averaging over time origins halfway through the data set. Increasing the averaging set to ¾ or even the entire data set, changed the results by roughly 10-20%. We found the strongest justification in stopping halfway through the data set, because stopping halfway through the data set would allow all values in the function to have an equal number of samples. Whether a purely numerical or physical effect, there is some basis for the function convergence, as further investigation was beyond the scope of our study. Nevertheless, we conducted simulations using simulation domains consisting of 4x4x4 and 6x6x6 unit cells corresponding to 512 and 1728 atoms respectively.

4.4 Relaxation Time Calculations

To calculate the phonon relaxation time in our simulations we not only considered various temperatures but also different crystallographic directions. In the approach outlined in chapter 3, we introduced the assumption of an isotropic crystal when discussing the density of states. To test the validity of the assumption we conducted simulations using rectangular domains with a redefined rectangular unit cell. This was done so that each crystal direction is aligned to the longest edge of the simulation domain. This approach was efficient in allowing extraction of the maximum number of normal modes per simulated atom along a particular crystal direction.

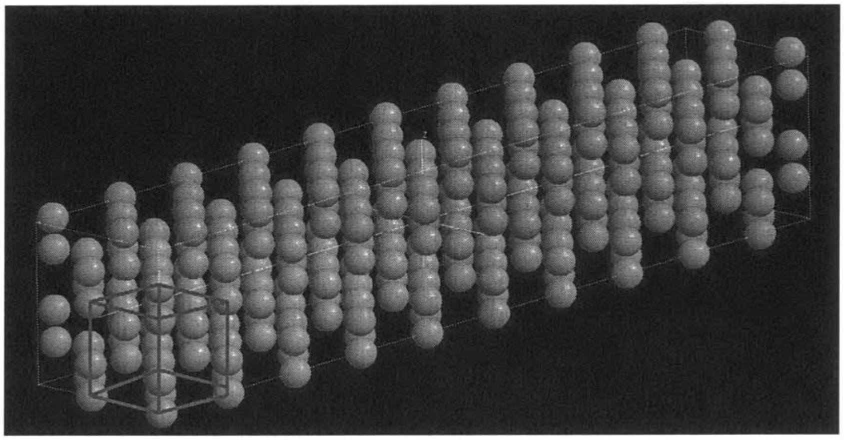

Figure 4.4.1 [1,0,0] Simulation domain

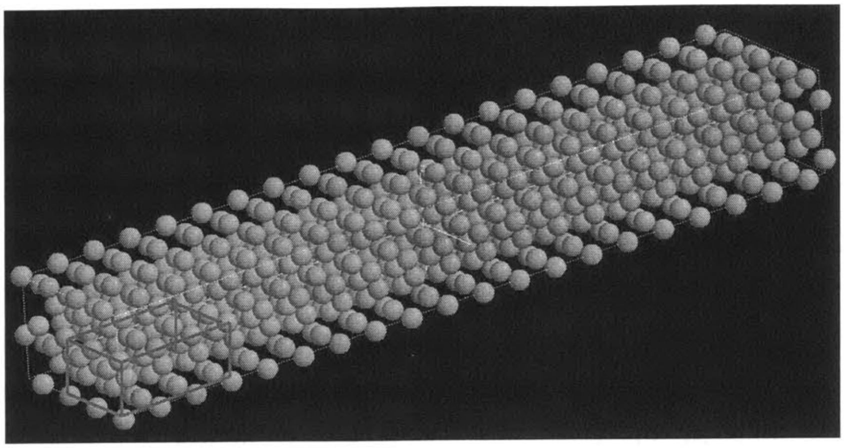

Figure 4.4.2 [1,1,0] Simulation domain

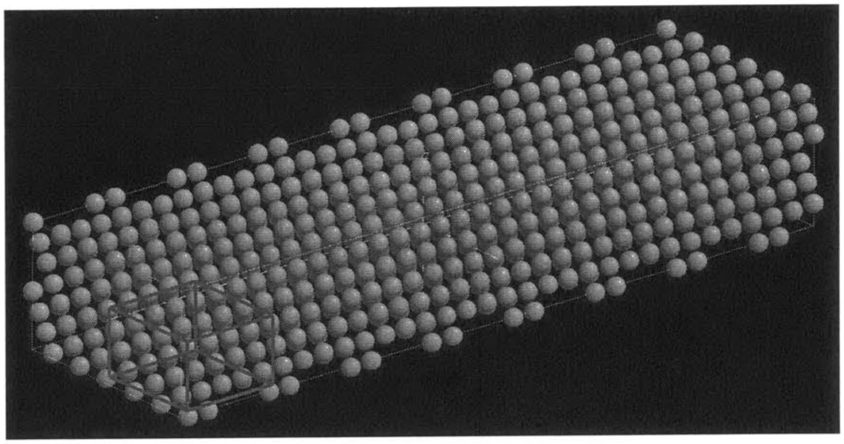

Figure 4.4.3 [1,1,1] Simulation domain

In our simulations we chose the [1,0,0], [1,1,0] and [1,1,1] directions for sampling, as the need for reorientation developed from the necessity to design shorter simulations with as many possible normal modes along the direction of interest. In preliminary calculations we encountered problems when extracting relaxation times from normal modes that did not repeat according to the periodic boundary conditions. The issue was resolved by selecting appropriate wavelengths that correspond to the simulation domain dimensions. In general we designed our simulations to include ten or more points within the Brillouin zone along each of these principal symmetry directions.

In our simulation, 3.3.4 was used to calculate the temporal normal mode amplitudes, while 3.4.4 was used to calculate relaxation times from the normal mode autocorrelation functions. In practice we noticed that the normal modes decayed over many oscillation periods and we could extract the phonon frequency directly from the average period spacing. The relaxation times were then calculated by least squares fitting of an exponential through the peaks of the normal mode autocorrelations. In preliminary calculations using five nanoseconds of simulation time we observed exponential decays, with clearly recognizable time constants. This served to initially validate the exponential decaying assumption in 3.4.3.

We reoriented the unit cells for two directions and kept the conventional unit cell for the [1,0,0] direction, where we used domains with 10x2x2 cells consisting of 320 atoms shown in figure 4.4.1. In preliminary testing we also noticed an interesting result, that within the statistical error there was no difference in the relaxation times when considering 10x3x3 (720 atoms) and 10x4x4 systems (1280 atoms). This suggests that the attenuation process is insignificantly related to the excitation of long wavelength modes in an orthogonal propagation direction. This could mean that most of the energy lost in an attenuating wave is converted to the excitation of short high frequency waves. Although interesting, the idea should be extensively tested to fully understand the phenomena. Using the 10x2x2 simulation domain, 10 normal modes that satisfy the boundary conditions were calculated, yielding 10 phonon frequencies and relaxation times. For the [1,1,0] direction we defined a unit cell with 16 atoms and simulated 10x2x2 systems consisting of 640 atoms, as shown in figure 4.4.2. This choice of domain size also provided 10 phonon frequencies and relaxation times. For the [1,1,1] direction a unit cell was defined that included 36 atoms, where we used 8x2x2 unit cells in the simulation domain consisting of 1,152 atoms shown in figure 4.4.3. This arrangement allowed us to calculate 12 phonon frequencies and relaxation times.

Once the frequencies and relaxation times were calculated they were averaged over five independent simulations and the data was used to calculate the thermal conductivity. In our methodology we essentially consider the limiting thermal conductivity of a perfect silicon crystal. We subsequently generated a set of 1000 frequencies between zero and 20THz to give sufficient resolution for all frequency dependent calculations. To convert the discrete dispersion and relaxation time data points to the higher resolution set, we linearly interpolated. For relaxation times corresponding to frequencies below the lowest data point in the MD dispersion, we used a $\frac{A_v(T)}{\omega^2}$ fit where $A_v(T)$ is a temperature and polarization dependent constant.[19] The constant $A_v(T)$ is determined by minimizing the least square error to the available data points, resulting in a smooth spectrum of relaxation times that accurately capture the higher frequency behavior where we interpolated.[19,56] Having outlined the procedures and parameters involved in our MD simulations we now move to a discussion of the results.

Chapter 5: Results and Discussion

In preceding chapters we described our motives and laid a theoretical framework for interpreting the trajectory of a MD simulation. In this chapter we examine the results of our simulations using EDIP to model silicon and shed light on the relaxation time, a component to the theory of phonons in solids that has been difficult to quantify. We start by examining our Green-Kubo results and then move to the relaxation time results. In this chapter we show frequency dependent results for the phonon specific heat, group velocity and relaxation time. This is then put into an isotropic averaged framework in order to identify the dominant phonon polarization and frequency dependent mean free path.

5.1 Green-Kubo Results

The theory and formalism for Green-Kubo thermal conductivity calculations was covered in chapter 3 and it has shown excellent agreement with experiments in other studies.[28,57-59] Others have used this formalism and found that increasing the simulation domain size subsequently increases the thermal conductivity calculation. This effect is attributed to the inclusion of longer phonon wavelengths within simulation domain and the diminishing effects of the periodic boundary conditions. The boundary condition seems to constrain the maximum phonon wavelength, but not the mean free path as we later show that the mean free path spans many periods of the simulation domain.

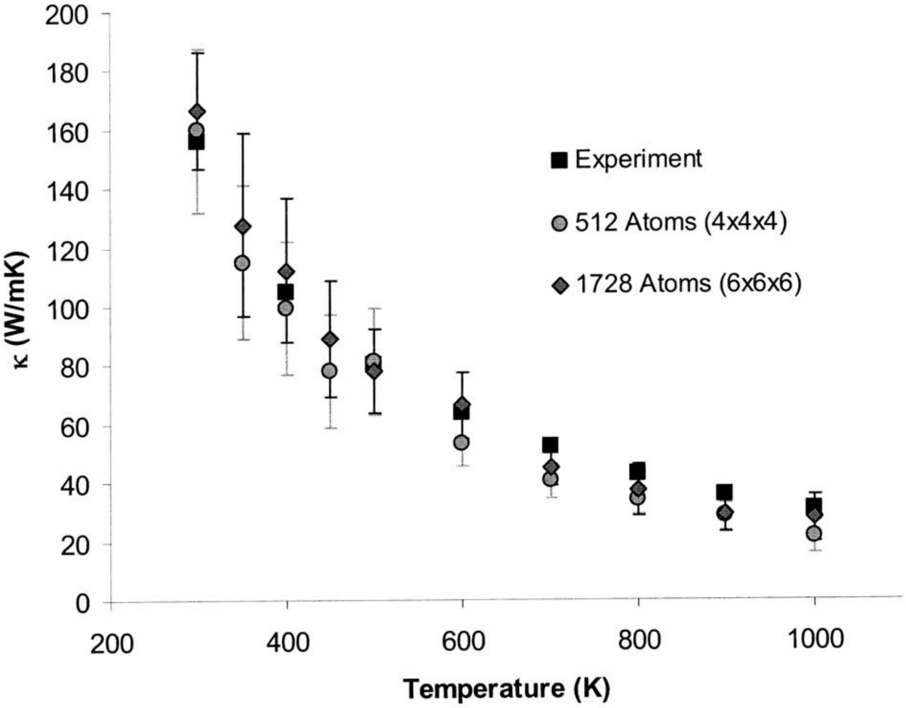

Figure 5.1.1 Green-Kubo Calculation of Thermal Conductivity

Figure 5.1.1 shows good agreement between the calculation and experiments,[21] where the values are in general higher for the larger 6x6x6 system. The error bars indicate ± the standard deviation over the five independent simulations, while the symbols indicate average values. These results add to the speculation that the phonon mean free path is not limited by the simulation cell size when using periodic boundaries. As will be shown in the sections to follow, the mean free path of phonons over most of the spectrum exceeds the largest domain dimension by orders of magnitude. We speculate that increasing the domain size would continue to increase the thermal conductivity up to the limiting value of a defect and impurity free single crystal silicon sample. The accurate magnitude and trend of the Green-Kubo results instills confidence in the forthcoming results for the BTE formulated analysis.

5.2 Density of States

As previously discussed we used lattice dynamics to calculate the phonon dispersion in different crystallographic directions. With this calculation we were able to associate each dynamical matrix eigenvector and eigenvalue with a particular polarization. As a result we calculated a density of states for all six individual polarizations, which allowed flexibility when performing the analysis to determine if a particular polarization dominates.

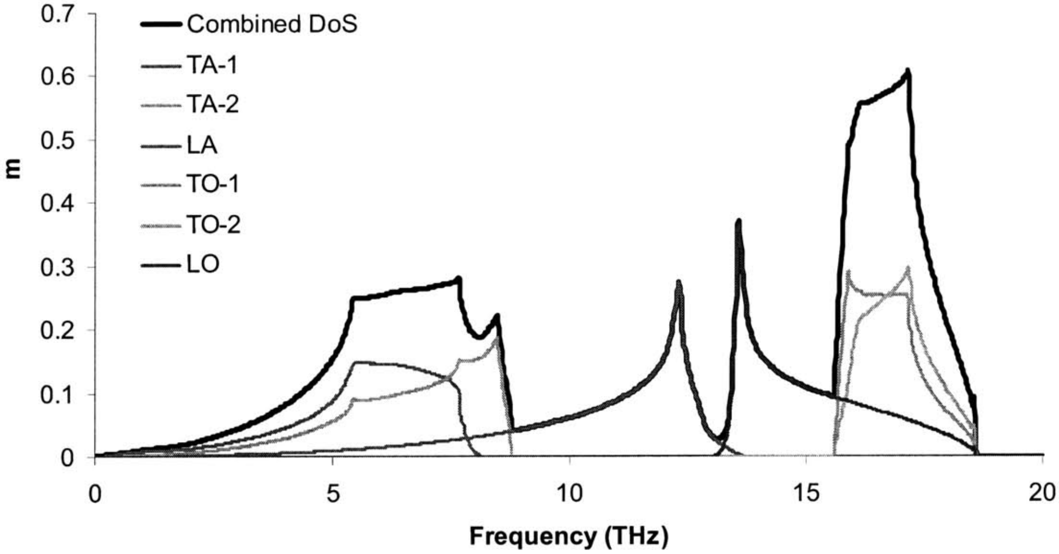

Figure 5.2.1 Phonon Density of States

Figure 5.2.1 shows the DoS for each polarization along with the combined function. In this, and all BTE related calculations to follow, we used an ω^2 fit to the density of states for the phonons below 0.5 THz. In conducting the calculation we sampled a Brillouin zone grid using 1000 factorial points, with 50,000 sampling points over 100 zone boundary intervals. Although the grid was fine we obtained small spikes for the very low frequencies due to the numerically discrete nature of the calculations. These spikes essentially grouped modes from a neighboring frequency bins into bins corresponding to the lowest sampled frequencies. This prohibited the density of states from smoothly decaying to zero. When combined with the divergent inverse frequency squared model for the relaxation times, the spikes caused significant errors in the calculations by attributing additional states to very long relaxation times. To remedy the problem we averaged our results with an ω^2 fit to cancel the effect and provide a smooth transition to zero.

5.3 Phonon Specific Heat

In deriving 3.4.18 we grouped the energy, distribution derivative and density of states together as the specific heat. This formulation allows us to illustrate an important view of the specific heat's temperature dependence, as it quantifies the amount of energy that phonons transfer in heat conduction.

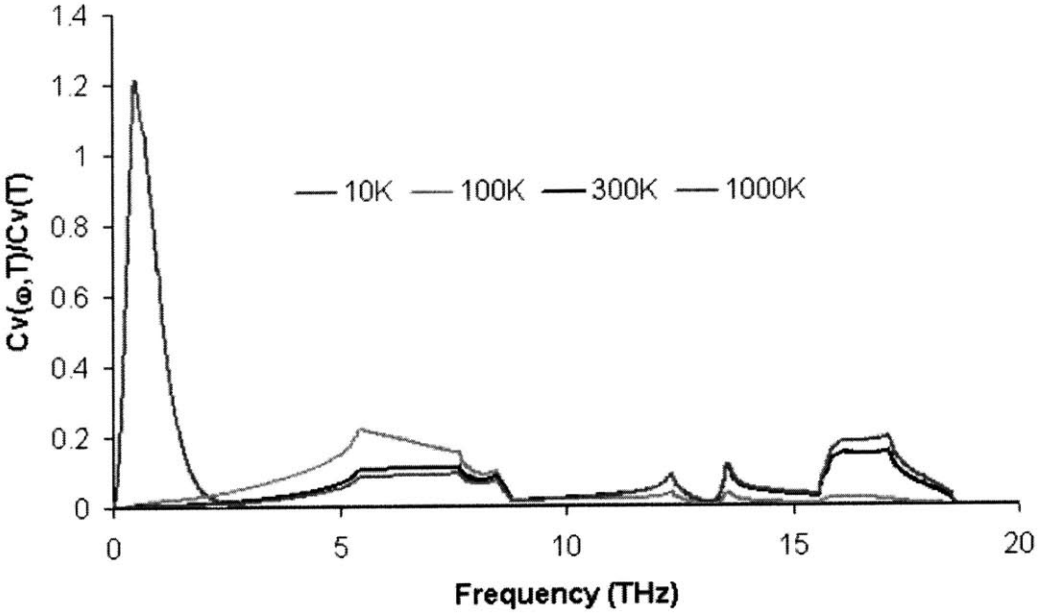

Figure 5.3.1 Specific Heat vs. Phonon Frequency at 10K, 100K, 300K and 1000K

Figure 5.3.1 illustrates how the spectral distribution of the energy allocation changes with respect to temperature. At low cryogenic temperatures, the low frequency phonons dominate and are allocated the greatest portion of the energy distribution. At moderate temperatures the spectrum spreads as the entire acoustic branches become active, while at room temperature the entire spectrum is active. This is an important feature, as the thermal conductivity essentially decreases after its peak around 40K because the spectrum spreads and low frequency phonons are no longer allocated the majority of the energy.

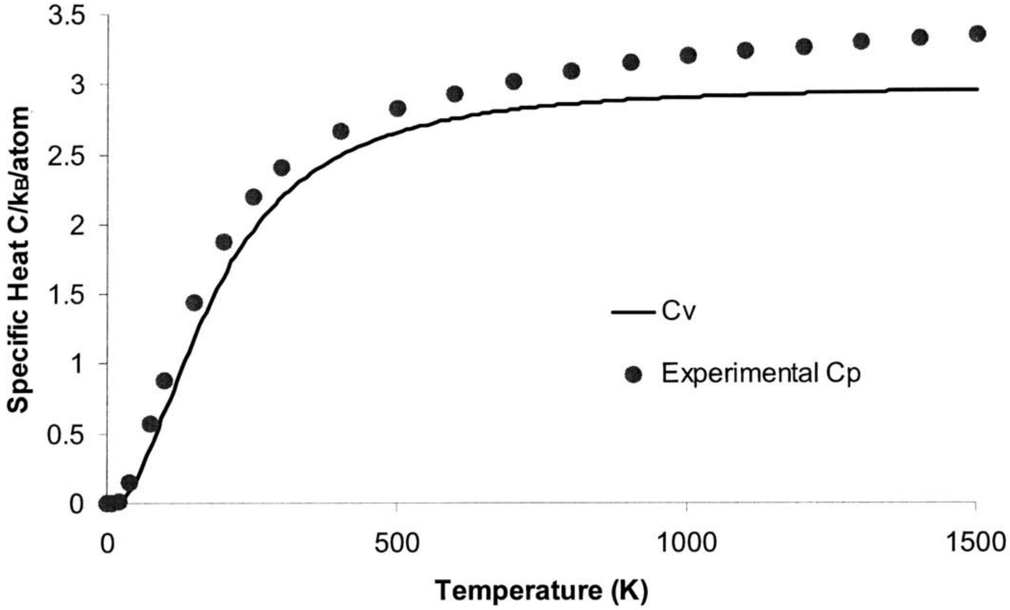

Figure 5.3.2 Silicon specific heat

As compared to experimental results,[60] figure 5.3.2 shows that our calculation agrees well over the entire temperature range considered, adding confidence to our results.

5.4 Phonon Group Velocity

In the BTE formalism, the appropriate velocity is the phonon group velocity, which describes the speed of a wave packet, centered about a particular phonon frequency. To calculate the group velocity we use the derivative of frequency with respect to wave vector. To compute this derivative we first establish the wave vector dependence of the frequencies through the phonon dispersion.

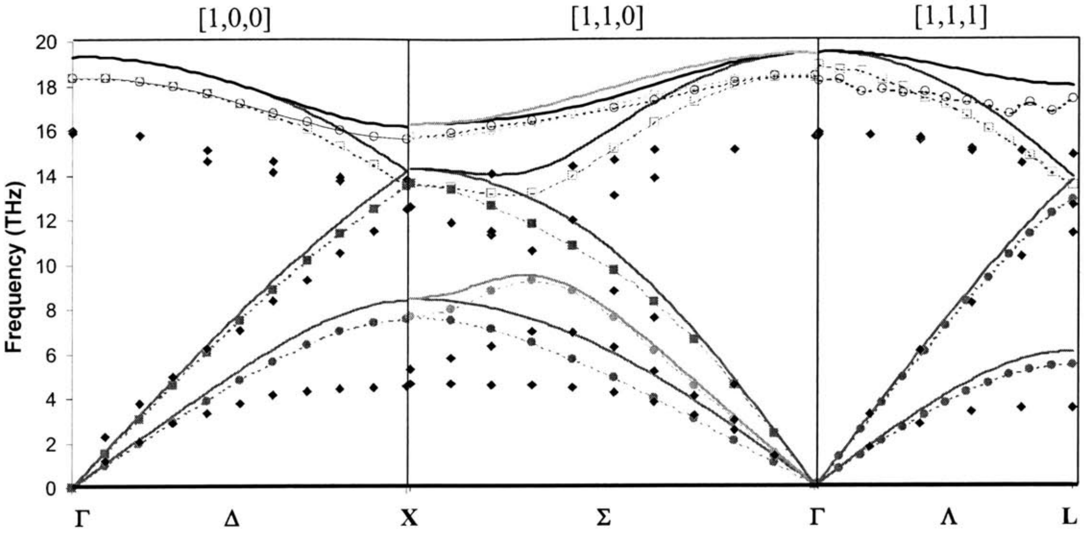

Figure 5.4.1 Phonon Dispersion: Lattice Dynamics (solid lines), Molecular Dynamics (dashed lines and symbols), Experiment (diamonds)

Figure 5.4.1 shows good agreement between the MD simulations and the lattice dynamics results, with the exception of the transverse optical frequencies in the [1,1,1] direction. There is reasonably good agreement between the model and experimentally observed values for silicon,[61-64] as EDIP appears to be overly stiff. This property of the potential is common to silicon potentials, as they tend to be overly stiff and exhibit higher frequencies. The additional stiffness is actually present in all of the branches, however the results do show the appropriate trends and profiles needed to determine accurate group velocities. To capture the slight temperature dependence of the group velocity we linearly interpolated between the dispersion points extracted from the MD simulations as opposed to using the lattice dynamics results.

5.5 Phonon Relaxation Time

Using previously outlined procedures we calculated relaxation times for phonons in different crystallographic directions and temperatures. The following figures summarize the results extracted from the MD simulations.

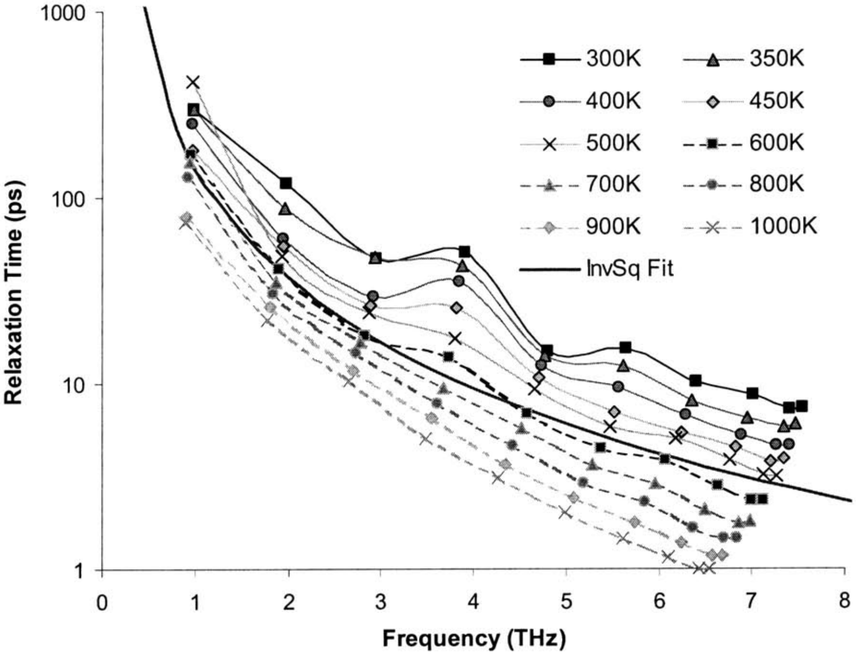

Figure 5.5.1 [1,0,0] Transverse Acoustic Relaxation Times

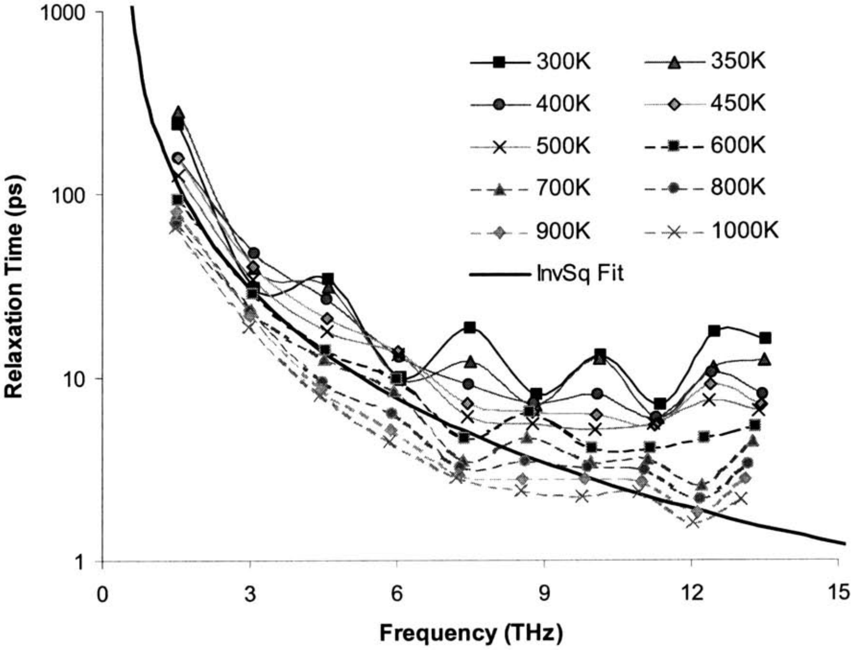

Figure 5.5.2 [1,0,0] Longitudinal Acoustic Relaxation Times

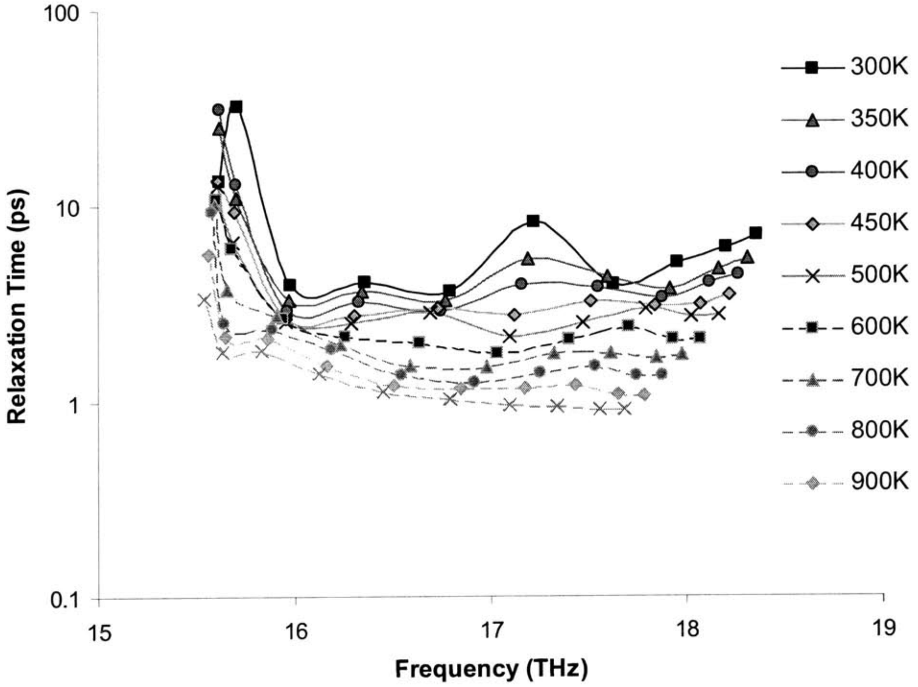

Figure 5.5.3 [1,0,0] Transverse Optical Relaxation Times

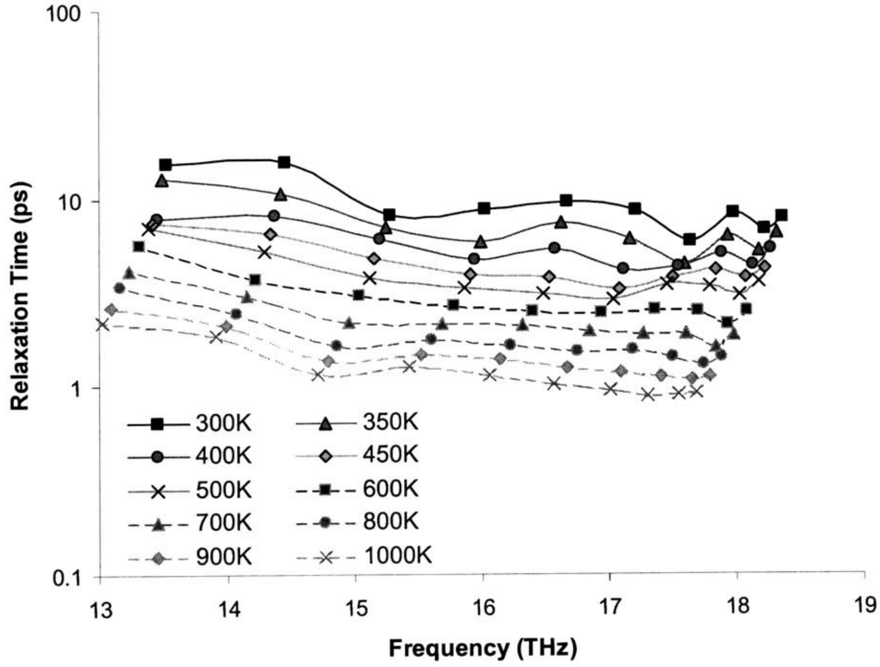

Figure 5.5.4 [1,0,0] Longitudinal Optical Relaxation Times

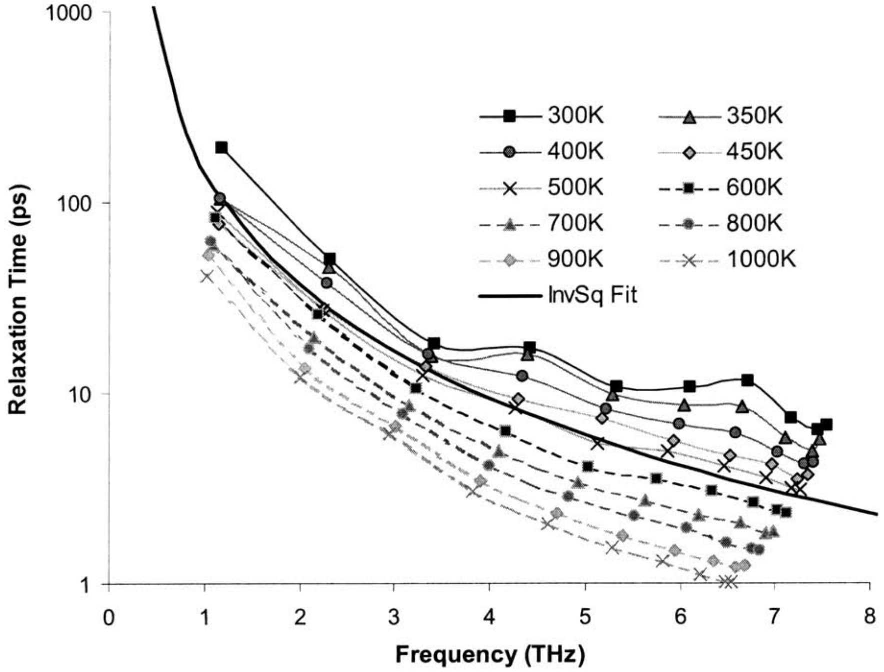

Figure 5.5.5 [1,1,0] Transverse Acoustic (1) Relaxation Times

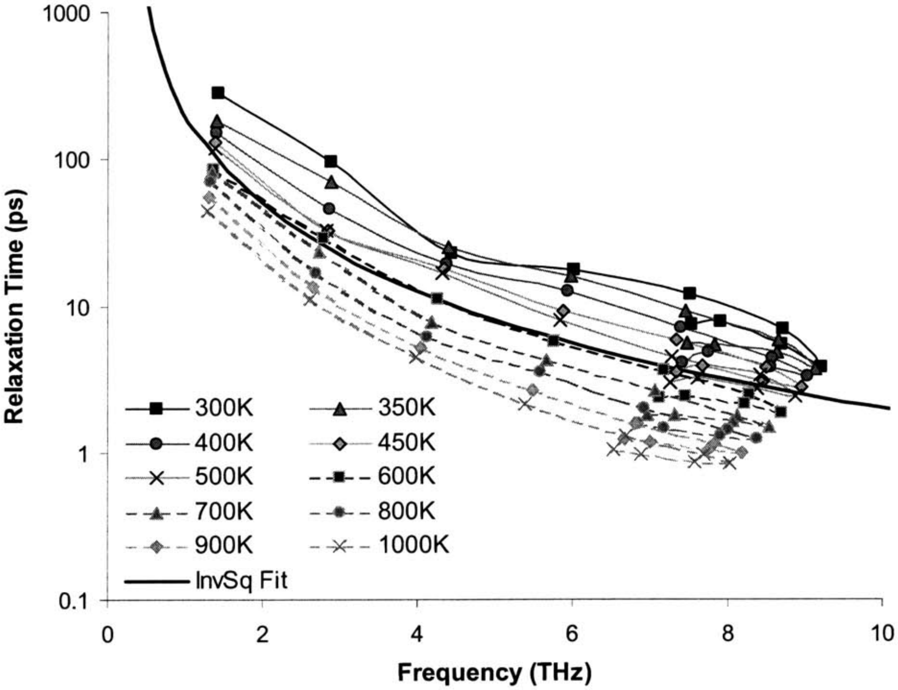

Figure 5.5.6 [1,1,0] Transverse Acoustic (2) Relaxation Times

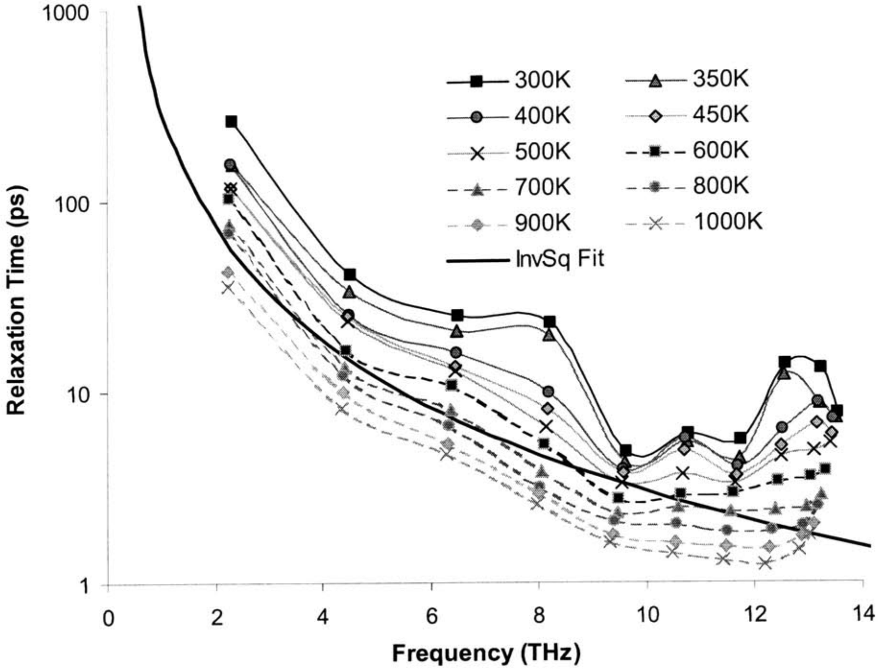

Figure 5.5.7 [1,1,0] Longitudinal Acoustic Relaxation Times

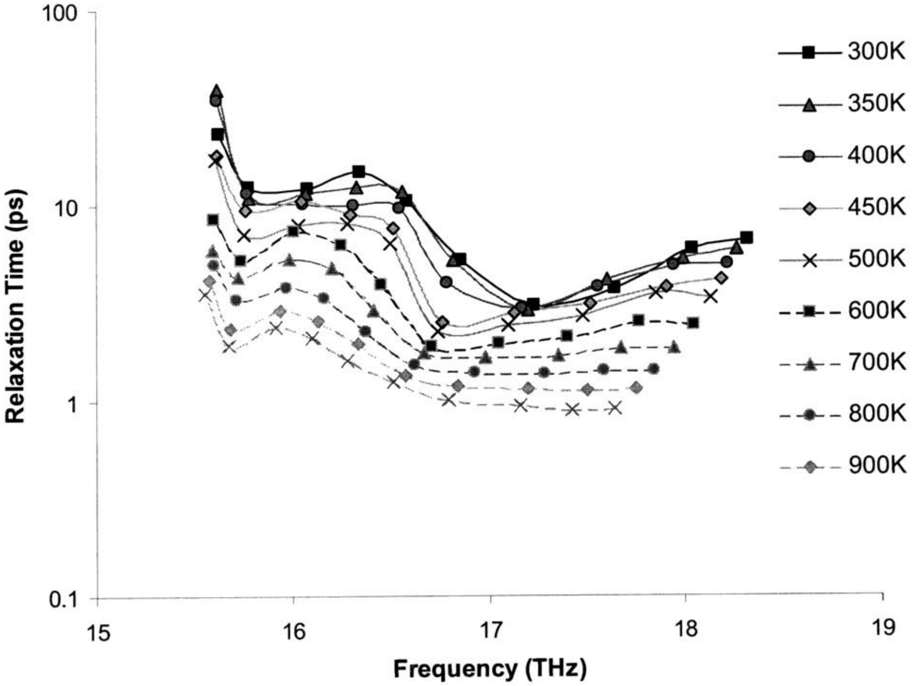

Figure 5.5.8 [1,1,0] Transverse Optical (1) Relaxation Times

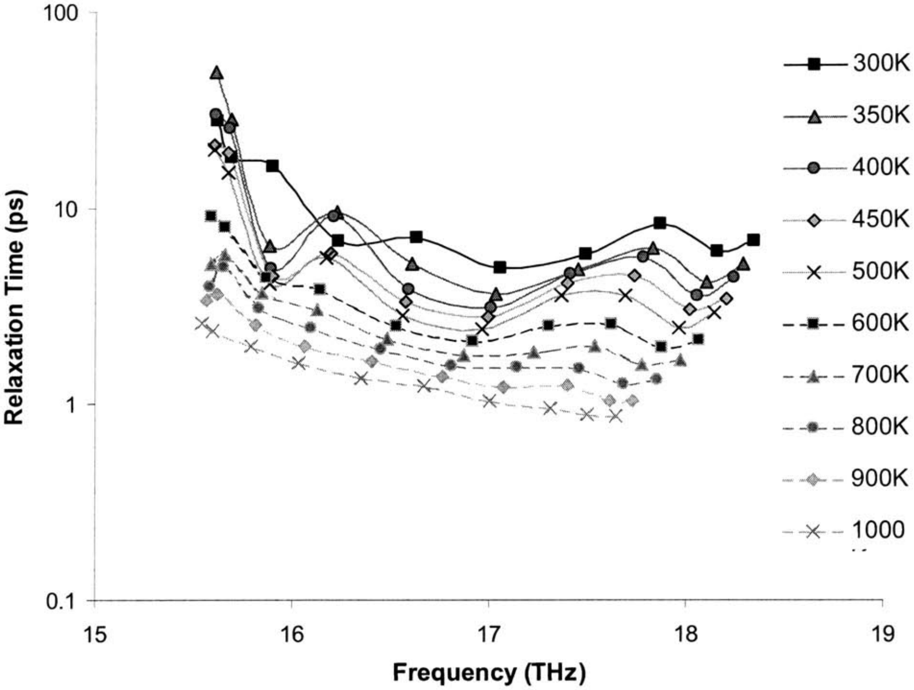

Figure 5.5.9 [1,1,0] Transverse Optical (2) Relaxation Times

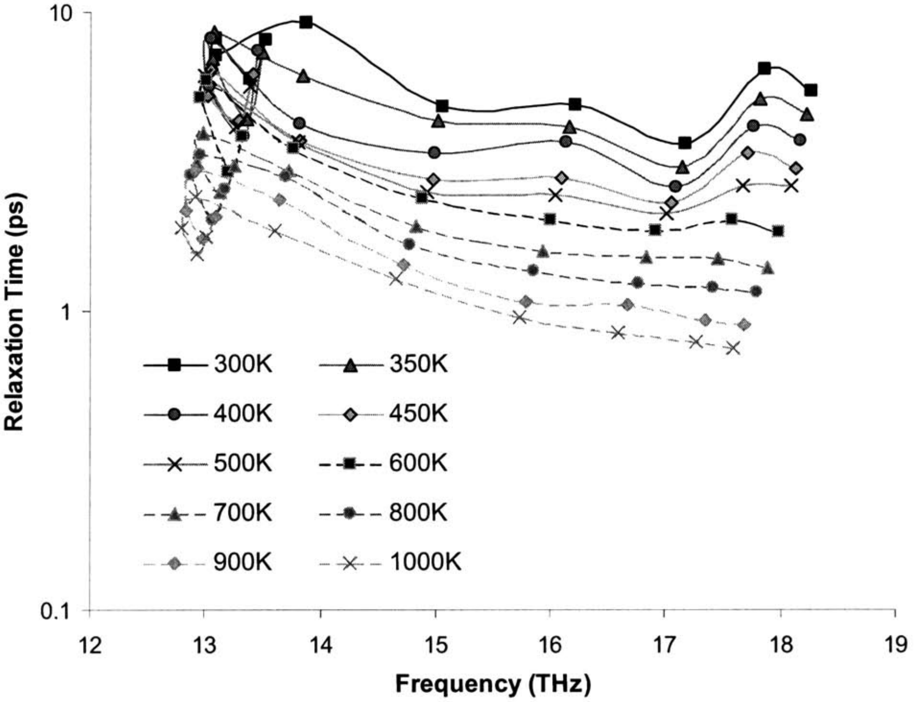

Figure 5.5.10 [1,1,0] Longitudinal Optical Relaxation Times

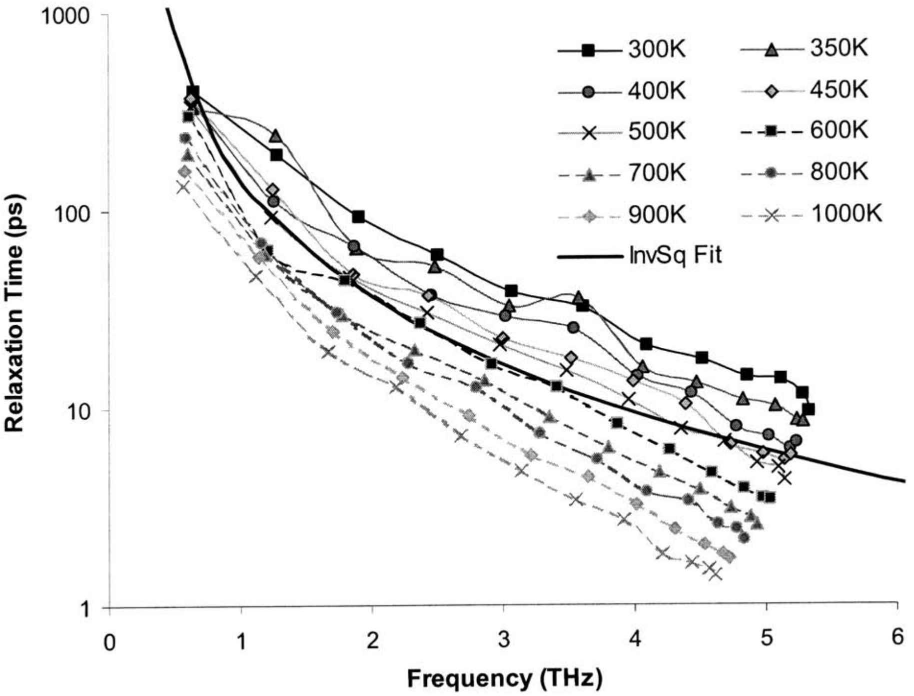

Figure 5.5.11 [1,1,1] Transverse Acoustic Relaxation Times

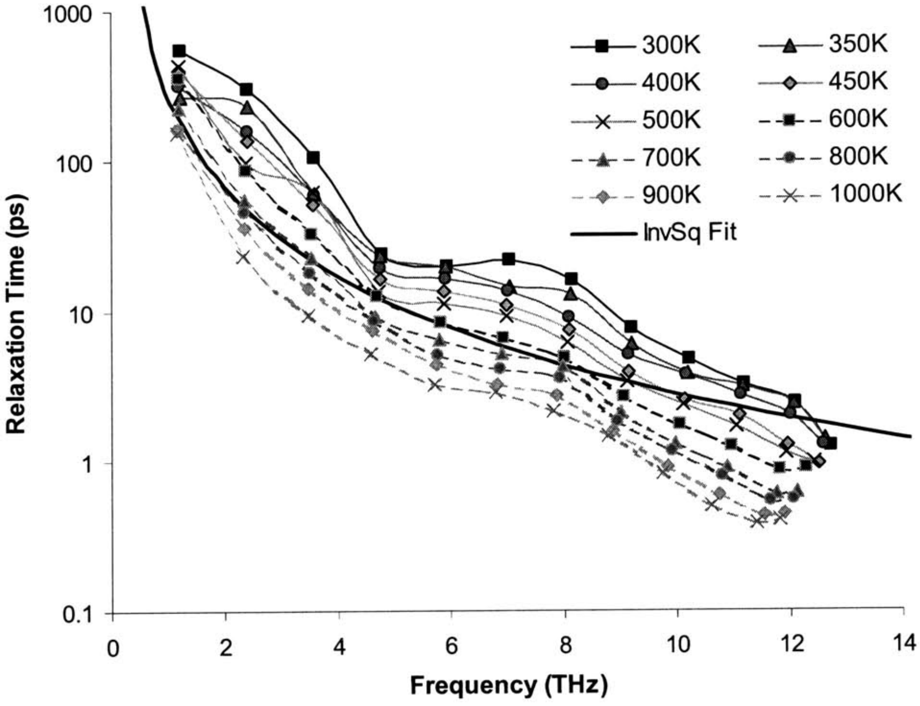

Figure 5.5.12 [1,1,1] Longitudinal Acoustic Relaxation Times

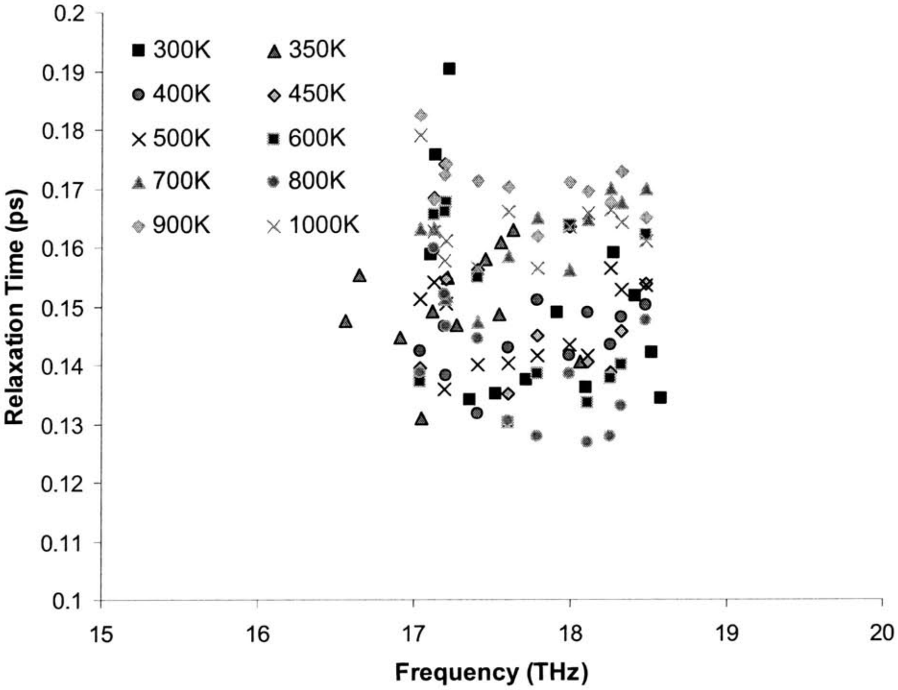

Figure 5.5.13 [1,1,1] Transverse Optical Relaxation Times

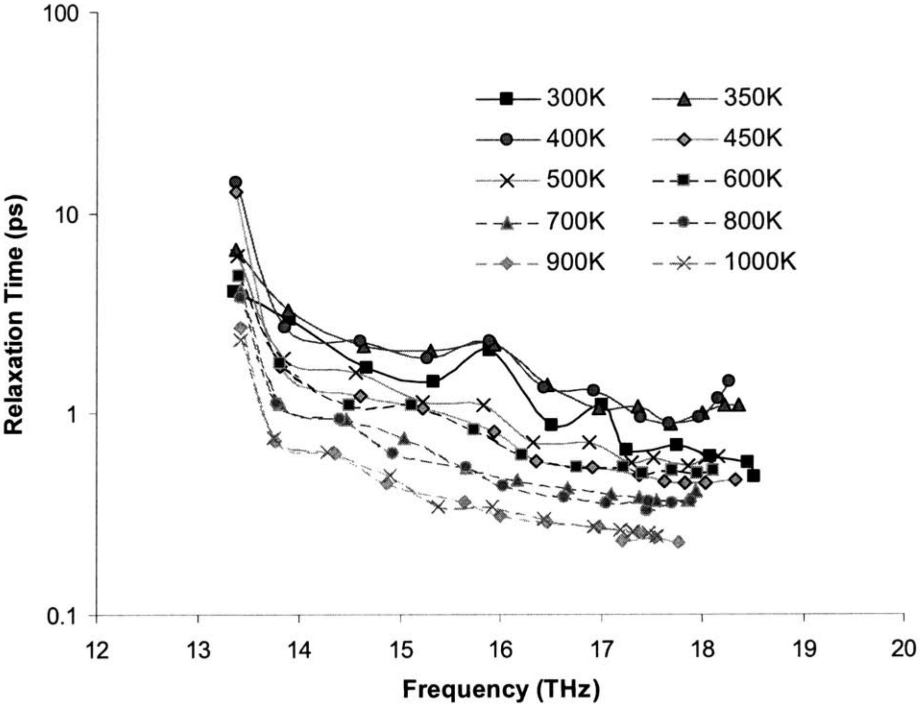

Figure 5.5.14 [1,1,1] Longitudinal Optical Relaxation Times

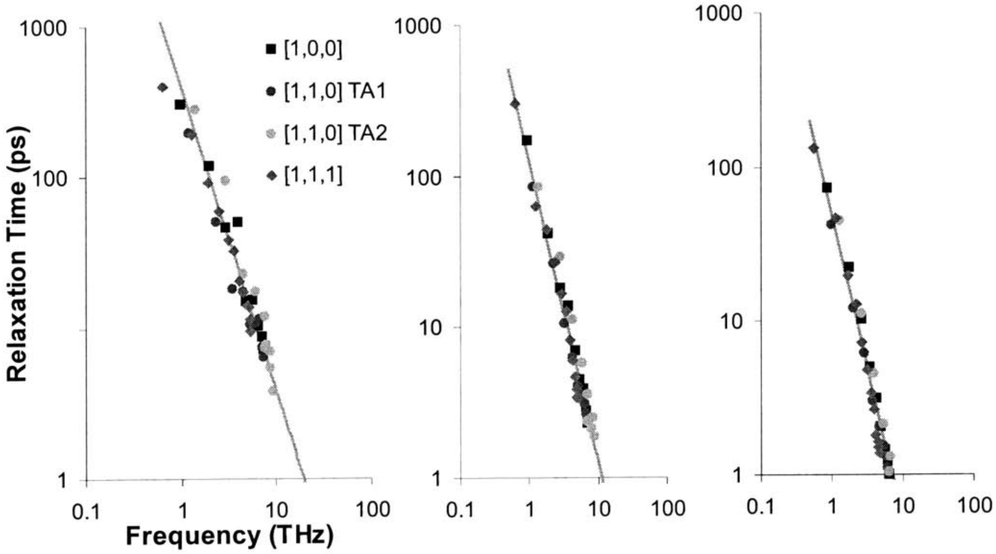

Figure 5.5.15 Transverse acoustic relaxation times at 300K, 600K and 1000K

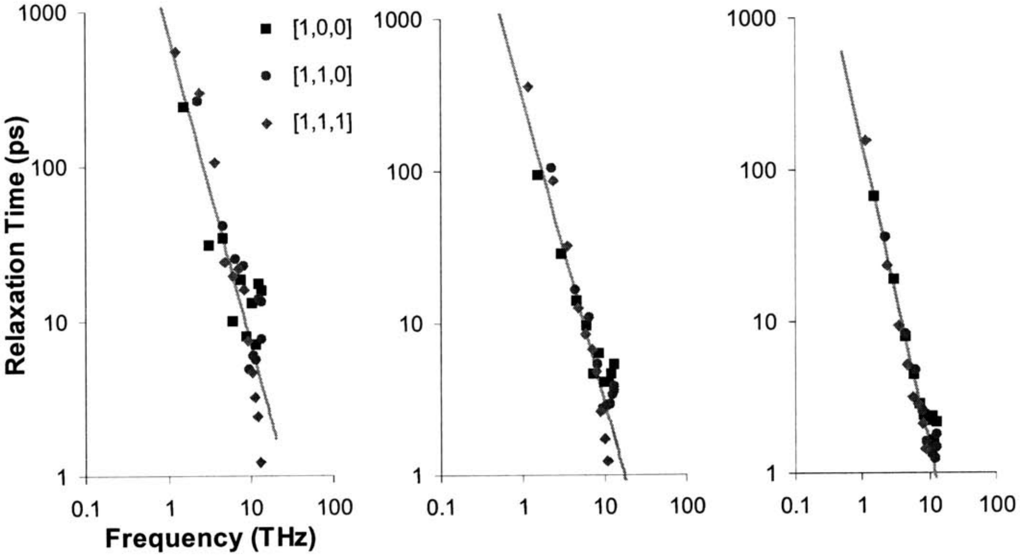

Figure 5.5.16 Longitudinal acoustic relaxation times at 300K, 600K and 1000K

The results show that treating the relaxation time proportional to $\frac{A_v(T)}{\omega^2}$ is a reasonable model, consistent with scattering theories[19] and the decay rate for audible sound wave attenuation.[56] For higher frequencies and particularly the optical modes, the trend deviates heavily from $\frac{A_v(T)}{\omega^2}$ and exhibits interesting features. For the transverse optical branch in [1,1,1] direction we observed inconsistent frequencies and very low relaxation times, which may possibly be due to coding errors. The values in the plots indicate averages over five sets of independent initial conditions while the error bars indicate the standard deviation among them. The general trends show that acoustic relaxation times are much larger than optical relaxation times. The longitudinal optical is also slightly larger than either of the transverse for all three of the principal directions. Since acoustic phonons have larger relaxation times and contribute the most to thermal transport, we place our emphasis on highlighting their properties.

Figures 5.5.15 and 5.5.16 help to justify our isotropic assumption. From the results it appears that the relaxation times in the principal directions are similar but have individual features towards the higher end frequencies. Although there is only moderate correspondence we see that the general trends are the same in each direction as the agreement increases with temperature. This lends moderate support to our isotropic assumption, as the relaxation time is most notably a function of frequency and does not exhibit heavy directional dependence. The differences amongst the branches can also be attributed to the momentum of the phonons. Since the zone boundaries are different for each direction, phonons with the same energy do not carry the same momentum, a conserved quantity in phonon-phonon scattering. Although the evidence here suggests that anisotropy in relaxation time is a tolerable assumption for silicon, it is not a general result, as we expect other non-cubic crystal structures to exhibit stronger directional dependence. The dispersion however is very anisotropic and has different shapes in each direction, giving rise to heavily direction dependent group velocities.

5.6 Isotropically Averaged Properties

Using Figures 5.5.16 and 5.5.17 to justify treating the phonon characteristics as isotropic, we examine the thermal conductivity under this assumption using the properties from preceding sections.

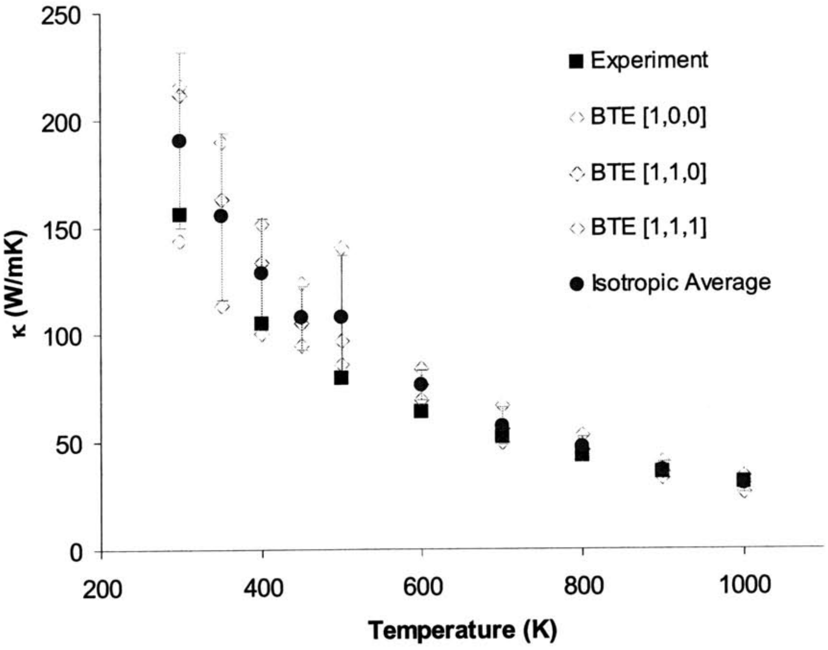

Figure 5.6.1 BTE Thermal Conductivity

Figure 5.6.1 shows that thermal conductivity, when using the isotropic averaged density of states with directionally dependent group velocity and relaxation time, yields a moderate spread of thermal conductivity values. However when averaged together, the values agree more closely with experiments, where we expected the values to be larger in our simulation of a perfect crystal. We also noticed an interesting feature that we ascribe to the potential, where there is a small deviation in the decreasing trend at 500K, also apparent in the Green-Kubo results. This may be the boundary of a threshold, beyond which increased nonlinearity in the potential decreases the thermal conductivity.

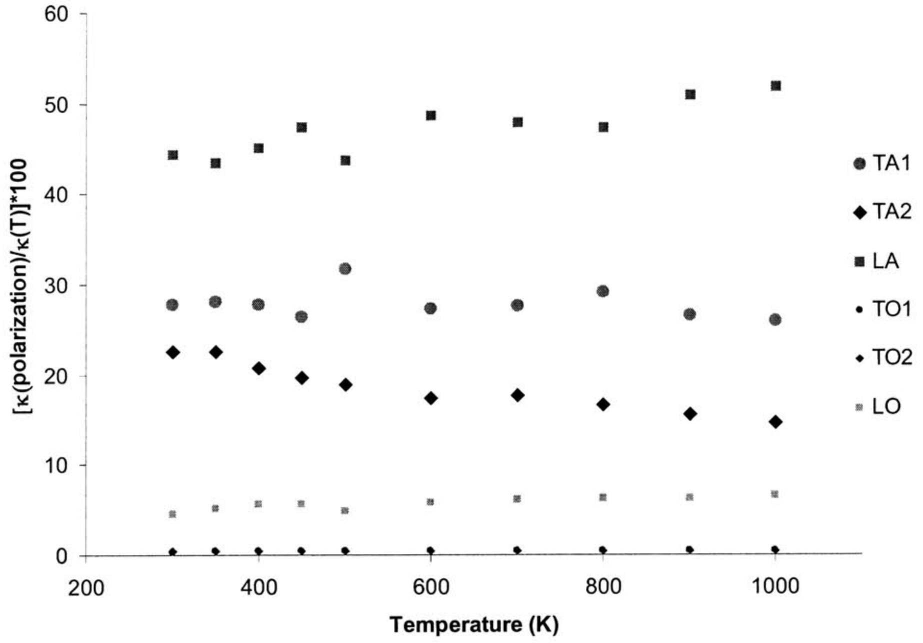

Figure 5.6.2 Contributions to thermal conductivity from different polarizations

Figure 5.6.2 reflects an interesting result, as it shows that the longitudinal acoustic mode contributes roughly 45% of the thermal conductivity, while the strongest transverse branch contributes about 30%. This clearly identifies the longitudinal acoustic polarization as the dominant mode of heat conduction in silicon. This trend was also found in another study using solid argon,[28] as we expect this may be a dominant trend in many materials. In general it appears that with respect frequency the longitudinal acoustic relaxation times are slightly larger than the transverse, however if plotted against wave vector the plots would share more coincidence. It is typical in many materials for the longitudinal acoustic branches to have a steeper slope and subsequently higher zone boundary frequency. Thus for the same momentum, longitudinal modes generally carry more energy, travel faster and have slightly longer relaxation times. The main feature that gives the longitudinal modes their dominance is the group velocity, which is squared in the thermal conductivity expression.

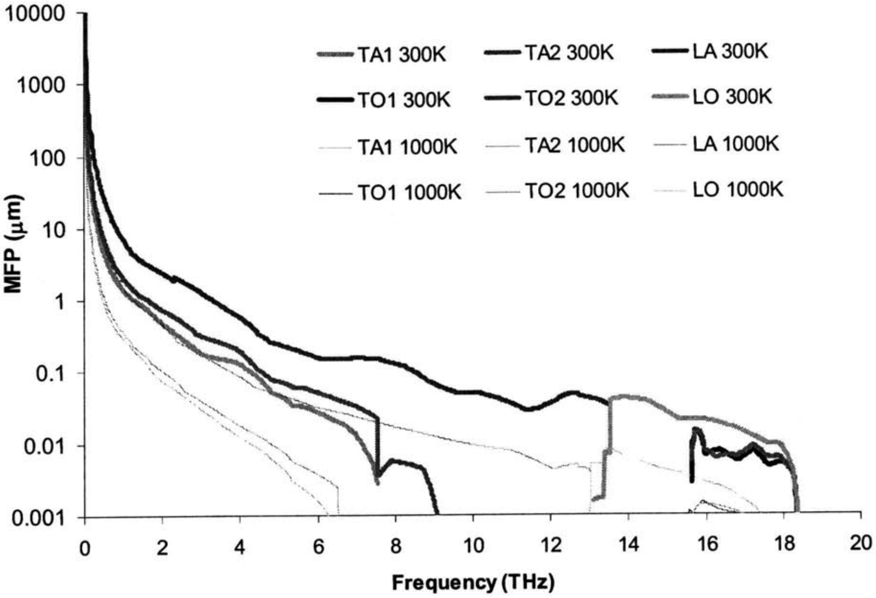

Figure 5.6.3 Isotropic averaged phonon mean free path spectrum at 300K and 1000K

Having identified the dominant polarization, we now examine the phonon mean free path. As discussed in chapter 1, our intention for this type of analysis is for understanding transport in nanostructures. Figure 5.6.3 clearly shows the regime in where we expect to see thermal conductivity reduction due to classical size effects. One interesting feature is that boundaries in nanostructures with dimensions below 10 nm, at room temperature, obstruct the propagation of all acoustic phonons. Since the optical phonons make up roughly 10% of the thermal conductivity we expect that the vibration dynamics in such small structures would be drastically different from bulk.

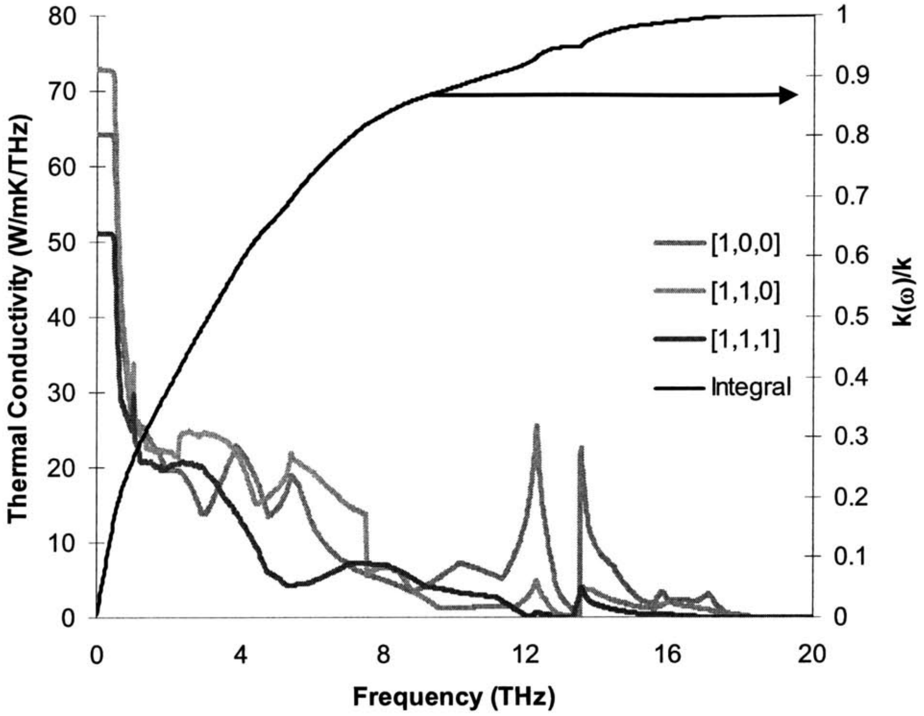

Figure 5.6.4 Thermal conductivity spectrum and aggregate integral at 300K

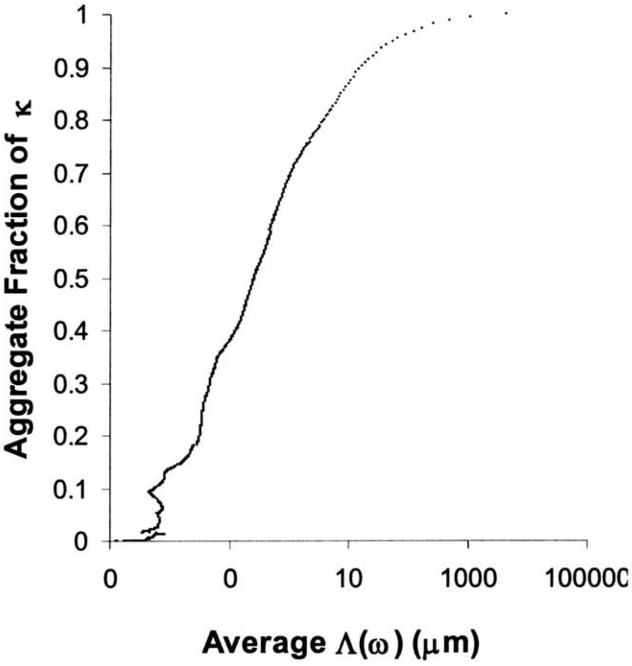

Figure 5.6.5 Thermal conductivity integral with corresponding mean free path at 300K

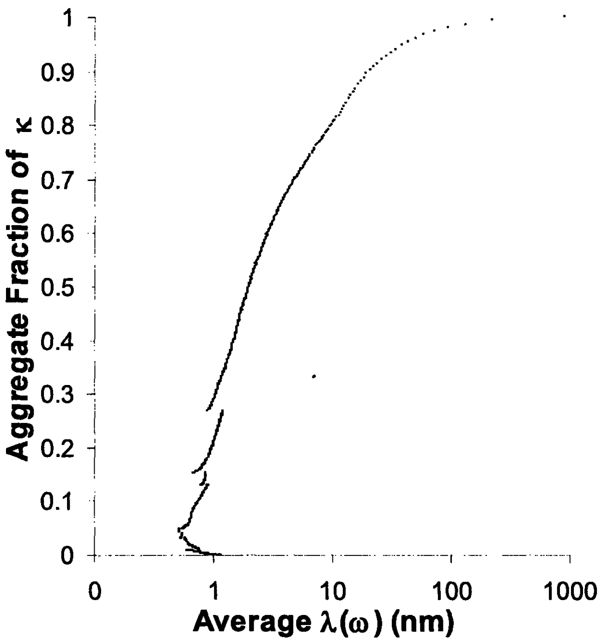

Figure 5.6.6 Thermal conductivity integral vs. phonon wavelength at 300K

To illustrate this effect we plot the thermal conductivity spectral contributions and the aggregation of the frequency dependent integral for the three directions in Figure 5.6.4. This plot shows that the contribution of low frequency phonons affected by the DoS ω^2 fitting is roughly 10% of the thermal conductivity at room temperature. The size effects are most apparent in figure 5.6.5 which shows the corresponding mean free paths associated with the integral. The figure shows that phonons traveling beyond 10 micron, a typical grain size for silicon crystals, contribute about 15% to the thermal conductivity. Thus from our study we quantify how decreasing the size of silicon nanostructures decreases the thermal conductivity by orders of magnitude. Figure 5.6.6 plot the thermal conductivity integral against the average phonon wavelength at the corresponding frequency. This shows that phonons with wavelengths shorter than 10 nanometers, approximately 20 unit cells, are responsible for 80% of the thermal transport in silicon. This is an interesting result indicating a length scale where size effects would heavily restrict the allowable modes to reduce thermal conductivity.

Conclusion

To study phonon heat conduction in bulk silicon we have derived and implemented two approaches using molecular dynamics simulations. The Green-Kubo approach, although accurate for calculating thermal conductivity, offers limited insight into heat conduction mechanisms. As a result, we also used a relaxation time approach based on the BTE that provides a more detailed picture. Previous works derived approximations for the frequency and temperature dependence of relaxation times, but confirmation through quantitative was lacking. The most prevalent, unresolved issue with previous studies was quantification of relative contributions from different phonon polarizations. In this thesis we described and demonstrated methods for analyzing phonon transport, resulting in the temperature and frequency dependent contributions to thermal conductivity.

Using both approaches we investigated silicon, which has been extensively studied because of its technological significance. Both thermal conductivity calculations agree with experiments, where the BTE results represent the limit of a perfect crystal. By extracting relaxation times from simulations, we generated quantitative validation to the theory of lattice thermal conductivity. Having also quantified the relative contributions from different polarizations, our results can also add to the understanding of phonon interactions.

The results of our simulations of silicon indicate that longitudinal acoustic modes are most dominant in the energy transport. Although the significance of these modes has been debated, our results provide quantitative evidence to confirm their importance. The dominance of longitudinal acoustic modes is primarily attributed to their group velocities, which are typically larger in many crystals. The acoustic relaxation times exhibit the strong frequency dependence predicted by Klemens, however the temperature dependence was $\tau \propto T^{-1.5}$. Optical relaxation times did not show strong frequency dependence, but shared the same temperature dependence as acoustic modes. As a result of their low group velocities, our calculations suggest that optical phonons contribute less than 10% to energy transport in silicon.

By simulating silicon in the diamond structure and reorienting the simulation domain we extracted relaxation times along each on the principal symmetry directions. Our results show moderate isotropic behavior with less deviation at higher temperatures. By interpolating and applying an ω^{-2} fit for low frequency phonon relaxation times, we calculated mean free paths spanning eight orders of magnitude at room temperature. The large spread is a consequence of the low frequency divergence within the ω^{-2} model. Our result stresses the importance of considering the frequency character of mean free paths, as simplified frequency averaged models can lead to significant errors. Neglecting the spectrum of mean free paths leads to under estimation of size effects and other related transport phenomena.

Plotting the aggregate thermal conductivity integral versus average mean free path showed that phonons that travel beyond 10 micron add 10% to the thermal conductivity. Although the ω^{-2} model diverges, diminishing number of states at low frequencies cancels the effect of long mean free paths, resulting in finite thermal conductivity. Plotting the aggregate integral versus average phonon wavelength also provides insight into the length scale where size effects could significantly limit the allowable modes. The results show that phonons shorter than 10 nanometers constitute 80% of thermal conductivity and thus dominate the transport. Having quantified the relative contributions to umklapp scattering, further study could be used to isolate effects from other scattering mechanisms. By quantifying these effects the accuracy of theories for boundary, interface, impurity and defect scattering can be tested, using comparative studies to determine frequency and temperature dependence. These results would lead to more detailed characterization of bulk materials and increased insight into the development of nanostructured materials.

References

1. Chen, G., Dresselhaus, M. S., Dresselhaus, G., Fleurial, J. P. and Caillat, T. Recent developments in thermoelectric materials. International Materials Reviews 48, 45 (2003).
2. Zhang, X. and Grigoropoulos, C. Thermal Conductivity and Diffusivity of Free-standing Silicon Nitride Thin Films. Review of Scientific Instruments 66, 1115 (1995).
3. Pearson, G. and Bardeen, J. Electrical Properties of Pure Silicon and Silicon Alloys Containing Boron and Phosphorous. Physical Review 75, 865 (1949).
4. Ruf, T., Henn, R., Asen-Palmer, M., Gmelin, E., Cardona, M., Pohl, H., Devyatych, G. and Sennikov, P. Thermal Conductivity of Isotropically Enriched Silicon. Solid State Communications 115, 243 (2000).
5. Seto, J. The Electrical Properties of Polycrystalline Silicon Films. Journal of Applied Physics 46, 5247 (1975).
6. Fabian, J. and Allen, P. Anharmonic Decay of Vibrational States in Amorphous Silicon. Physical Review Letters 77, 3839 (1996).
7. Lu, X. and Chu, J. Phonon Heat Transport in Silicon Nanowires. European Physical Journal B 26, 375 (2002).
8. Ju, Y. and Goodson, K. Phonon Scattering in Silicon Films with Thickness of Order 100nm. Applied Physics Letters 74, 3005 (1999).
9. Scholten, A. and Dijkhuis, J. Decay of High Frequency Phonons in Amorphous Silicon. Physical Review B 53, 3837 (1996)
10. Tamura, S. Quasidiffusive Propagation of Phonons in Silicon: Monte Carlo Calculations. Physical Review B 48, 13502 (1993).
11. Gesele, G., Linsmeier, J., Drach, V., Fricke, J. and Arens-Fischer, J. Temperature-dependent Thermal Conductivity of Porous Silicon. J. Phys. D: Appl. Phys. 30, 2911 (1997).
12. Volz, S. and Chen, G. Molecular-dynamics simulation of Thermal Conductivity of Silicon Crystals. Physical Review B 61, 2651 (2000).

13. Nolas, G. S., Sharp, J. and Goldsmid, H. J. Thermoelectrics: Basic Principles and New Materials Developments (Springer, 2001).
14. Ashcroft, N. and Mermin, N. Solid State Physics (Thomson Learning, 1976)
15. http://www.tetech.com/ accessed on 5/2/06
16. Rowe, D. M. Handbook of Thermoelectrics (CRC Press, 1995).
17. Incropera, F. P. and DeWitt, D. P. Fundamentals of Heat and Mass Transfer (Wiley, 1996).
18. Yang, R. and Chen, G. Thermal conductivity modeling of periodic two-dimensional nanocompoites. Physical Review B 69, 195316 (2004).
19. Klemens, P. Thermal Conductivity and Lattice Vibrational Modes. Solid-State Physics Vol 7 (1958).
20. Chen, G. Nanoscale Energy Transport and Conversion (Oxford University Press, 2005)
21. Glassbrenner, C. J. and Slack, G. Thermal Conductivity of Silicon & Germanium from 3K to the Melting Point. Physical Review 134, 4A 1058 (1963).
22. Thacher, P. Effect of Boundaries and Isotopes on the Thermal Conductivity of LiF. Physical Review 156, 975 (1967).
23. Yim, W., Fitzke, E. and Rosi, R. Thermoelectric Properties of Bi2Te3-Sb2Te3-Sb2-Se3 Pseudo-ternary Alloys in the Temperature Range 77- 300K. Journal of Materials Science 1, 52 (1966).
24. Li, D., Wu, Y., Kim, P., Shi, L., Yang, P. and Majumdar, A., Thermal Conductivity of Individual Silicon Nanowires. Applied Physics Letters 83, 2934 (2003).
25. Yamasaki, I., Yamanaka, R., Mikami, M., Sonobe, H., Mori, Y. and Sasaki, T., Thermoelectric Properties of Bi2Te3/Sb2Te3 Superlattice Structure. Proc. 17th International Conference on Thermoelectrics 0-7803-4907-5/98.
26. Schmid, M., Hebenstreit, W., Varga, P. and Crampin, S. Quantum Wells and Electron Interference Phenomena in Al due to Subsurface Noble Gas Bubbles. Physical Review Letters 76, 2298 (1996).
27. Frenkel, D. and Schmidt, B. Understanding Molecular Simulation (Academic Press, 1996)

28. McGaughey, A. and Kaviany, M. Quantitative Validation of the Boltzmann Transport Equation Phonon Thermal Conductivity Model Under the Single Mode Relaxation Time Approximation. Physical Review B 69, 094303 (2004).
29. Branka, A., Kowalik, M. and Wojciechowski, K. Generalization of the Nose-Hoover Approach. Journal of Chemical Physics 119, 1929 (2003).
30. Inoue, R., Tanaka, H. and Nakanishi, K. Molecular Dynamics Study of the Anomalous Thermal Conductivity of Clathrate Hydrates. Journal of Chemical Physics 104, 9569 (1996).
31. Maeda, A. and Munakata, T., Lattice Thermal Conductivity via Nonequilibrium Molecular Dynamics. Physical Review E 52, 234 (1995).
32. Mountain, R. and MacDonald, R. Thermal Conductivity of Crystals: A Molecular Dynamics Study of Heat Flow in a Two Dimensional Crystal. Physical Review B 28, 3022 (1983).
33. Muller-Plathe, F. A Simple Nonequilibrium Method for Calculating the Thermal Conductivity. Journal of Chemical Physics 106, 6082 (1997).
34. Berber, S., Kwon, Y. and Tomanek D. Unusually High Thermal Conductivity of Carbon Nanotubes. Physical Review Letters 84, 4613 (2000).
35. Maruyama, S. and Kimura, T. A Study on Thermal Resistance Over a Solid-Liquid Interface by the Molecular Dynamics Method. Thermal Science and Engineering 7, 63 (1999).
36. Volz, S., Saulnier, J., Lallemand, M., Perrin, B., Depondt, P. and Mareschal, M. Transient Fourier-law Deviation by Molecular Dynamics in Solid Argon. Physical Review B 54, 340 (1996).
37. Kohn, W., Becke, A. and Parr, R. Density Functional Theory of Electronic Structure. Journal of Physical Chemistry 100, 12974 (1996).
38. Giannozzi, P., Grioncoli, S., Pasquale, P. and Baroni, S. Ab initio Calculation of Phonon Dispersions in Semiconductors. Physical Review B 43, 7231 (1991)
39. Kresse, G. and Hafner, J. Ab Initio Molecular Dynamics for Liquid Metals. Physical Review B 47, 558 (1993).
40. Laasonen, K., Sprik, M. and Parrinello, M. Ab Initio Liquid Water. Journal of Chemical Physics. 99, 9080 1993.

41. Baroni, S. and Resta, R. Ab Initio Calculation of Dielectric Constant in Silicon. Physical Review B 33, 7017 (1986).
42. Wang, C., Chan, C. and Ho, K. Tight-binding Molecular-Dynamics Study of Defects in Silicon. Physical Review Letters 66, 189 (1991).
43. Csanyi, G., Albaret, T., Payne, M. and De Vita, A. "Learn-on-the-Fly": A Hybrid Classical and Quantum-Mechanical Molecular Dynamics Simulation. Physical Review Letters 93, 175503 (2004).
44. Ercolessi, F. and Adams, J. Interatomic Potentials from First Principals Calculations: the Force Matching Method. Europhysics Letters 26, 583 (1994).
45. Daw, M. and Baskes, M. Embedded-atom Method: Derivation and Application to Impurities, Surfaces and Other Defects in Metals. Physical Review B 29, 6443 (1984).
46. Stillinger, F. and Weber, T. Computer Simulation of Local Order in Condensed Phases of Silicon. Physical Review B 31, 5262 (1985).
47. Tersoff, J. New Empirical Model for the Structural Properties of Silicon. Physical Review Letters 56, 632 (1986).
48. Justo, J., Bazant, M., Kaxiras, E., Bulatov, V. and Yip, S. Interatomic Potential for Silicon Defects and Disordered Phases. Physical Review B 58, 2539 (1998).
49. Woolley, R. The Dependence of Cluster Binding Energy on Coordination Number Z. J. Phys. B: At. Mol. Opt. Phys. 23, 1563 (1990).
50. Dove, M., Introduction to Lattice Dynamics (Cambridge University Press, 1993)
51. Harris, S., An Introduction to the Theory of the Boltzmann Equation (Holt, Rinehart and Winston Inc., 1971)
52. Hardy, R. Energy Flux Operator for a Lattice. Physical Review 132, 168 (1963)
53. Ladd, A., Moran, B. and Hoover, W. Lattice Thermal Conductivity: A Comparison of Molecular Dynamics and Anharmonic Lattice Dynamics. Physical Review B 34, 5058 (1986).
54. http://www-math.mit.edu/~bazant/EDIP/ accessed on 5/2/06
55. Okada, Y. and Tokumaru, Y. Precise Determination of Lattice Parameter and Thermal Expansion Coefficient of Silicon Between 300K and 1500K. Journal of Applied Physics 56, 314 (1984).

56. Szabo, T. Causal Theories and Data for Acoustic Attenuation Obeying a Frequency Power Law. J. Acoust. Soc. Am. 97, 14 (1995).
57. Lee, Y., Biwas, R., Soukoulis, C., Wang, C., Chan, C. and Ho, K. Molecular Dynamics Simulation of Thermal Conductivity in Amorphous Silicon. Physical Review B 43, 6573 (1991).
58. Che, J., Cagin, T., Deng, W. and Goddard, W. Thermal Conductivity of Diamond and Related Materials from Molecular Dynamics Simulations. Journal of Chemical Physics 113, 6888 (2000).
59. Lindand, P. and Gillan, M. A Molecular Dynamics Study of the Thermal Conductivity of CaF2and UO2. Journal of Physics and Condensed Matter 3, 3929 (1991).
60. Hultgren, R., Desai, P., Hawkins, D., Gleisser, M., Kelley, K. and Wagman, D. Selected Values of Thermodynamic Properties of the Elements (American Society for Metals, 1973)
61. Nilsson, G. and Nelin, G. Study of Homology Between Silicon and Germanium by Thermal-Neutron Spectrometry. Physical Review B 6, 3777 (1972).
62. Brockhouse, B. Lattice Vibrations in Silicon and Germanium. Physical Review Letters 2, 256 (1959).
63. Kulda, J., Strauch, D., Pavone, P. and Ishii, Y. Inelastic-Neutron-Scattering Study of Phonon Eigenvectors and Frequencies in Si. Physical Review B 50, 13347 (1994).
64. Holt, M., Wu, Z., Hong, H., Zschack, P., Jemian, P., Tischler, J., Chen, H. and Chiang, T. Determination of Phonon Dispersions from X-Ray Transmission Scattering: The Example of Silicon. Physical Review Letters 83, 3317 (1999).